Long-Term Non-Bleaching Nanoscale Imaging by Plasmonic Nanoscope

by

Xintao Zhao

A dissertation submitted in partial fulfillment
of the requirements for the degree of
Doctor of Philosophy
(Electrical and Computer Engineering)
in the University of Michigan
2024

Doctoral Committee:

Professor Somin Eunice Lee, Chair
Professor Sunitha Nagrath
Professor Louise Willingale
Professor Euisik Yoon

Xintao Zhao

xintao@umich.edu

ORCID iD: 0009-0007-5437-2239

ACKNOWLEDGMENTS

The work related to this thesis was funded by the Air Force Office of Scientific Research (AFSOR) and National Science Foundation (NSF). Firstly, I would like to express my deepest gratitude to my advisor Prof. Somin Eunice Lee for her invaluable advice, guidance, and encouragement during my PhD study. I am also thankful to Di Zu and Zhijia Zhang for their assistance in cell culture and long-term cell imaging. Special thanks to Ancheng Da and Guangjie Cui for their help on post image reconstruction and actin filament simulation. I would like to extend my sincere thanks to Guangjie Cui, Wei-kuan Lin and Zachary Burns for their contribution in gold nanorod synthesis, ligand exchange and gold nanorod functionalization. I'd like to also recognize Hojae Lee, John Gregg and Yonggil Jang for their initial help on actin filament fluorescent imaging, flow chamber setup, cell expansion and differentiation. Last, I could not have undertaken this journey without the support from my parents fand my partner.

TABLE OF CONTENTS

LIST OF FIGURES

FIGURES

LIST OF APPENDICES

APPENDIX

ABSTRACT

Long-term observation of live cells and activities, including cell dynamics and cellular responses, is a crucial technology in the field of cell studies such as cancer diagnostics and disease therapy. The challenges of long-term imaging fall under four categories: selection of cell type amenable to long-term imaging; precise control of the cellular environment under in-vitro system; imaging system and probe design to overcome photobleaching, phototoxicity, and to achieve high resolution; efficient data extraction and post data analysis process. Here we present a long-term non-bleaching nanoscale imaging method by plasmonic nanoscope. Through plasmonic molecular marker (gold nanorods) labeling and phase intensity separation of nanoprobes, we achieved non-bleaching, nanoscale imaging of biological systems, such as actin networks. While the standard fluorophore-based method limiting the imaging windows to minutes (< 1 hour), using our optimized imaging system, we were able to continuously observe long-term biological dynamics in the window of hours to days as well as achieving sub-10 nm resolution. The innovative nanoscale imaging system utilizing a plasmonic nanoscope has been successfully developed to address challenges encountered in long-term bio-imaging and demonstrated by visualization and quantitative analysis of actin dynamics during the disassembly process by actin binding protein (cofilin). Furthermore, we demonstrated live-cell imaging using nanoscale plasmonic nanoscope which allowed for the exploration of the orientation distribution of extracellular β-actin network within a cell-division cycle.

Chapter 1 Introduction

1.1 Long-term cell imaging

The exploration of cell studies, which yields invaluable insights and unravel the inherent heterogeneity within cell populations, are mostly conducted through snapshot analysis[1–5], by periodically imaging the samples in a longer time window. However, snapshots of a cell dynamics event, while informative, lacks temporal resolution and can sometimes lead to misinterpretations. These misinterpretations might arise from the same experimental dataset, generating alternative conclusions. To overcome this limitation, continuous analysis of single cell becomes imperative. This continuous observation is critical in decoding rare, dynamic, and heterogeneous cell responses that might otherwise remain unnoticed in population-based or snapshot single-cell analyses[6]. Notably, unlike many high-throughput techniques that require cell destruction for quantification, continuous long-term cell imaging offers a noninvasive approach. The essence lies in the necessity for prolonged, uninterrupted, and long-term observation of a cell across several cell divisions and over weeks. Only through this sustained monitoring can the temporal information essential for decoding the diverse responses of individual cells in distinct states be obtained[7–9].

In this chapter, I will delve into the challenges associated with long-term cell imaging. Specifically, I will discuss the state-of-the-art technologies addressing challenges related to molecular markers, environmental control, and imaging systems. These elements form integral components in ensuring the success and precision of long-term cell imaging techniques.

1.2 Challenges of long-term imaging

The pursuit of achieving successful long-term biological imaging involves navigating various challenges within the entire imaging system. These challenges encompass several critical aspects (Fig. 1.1). Firstly, it requires an optimal imaging environment that demands suitable culture surfaces or appropriate coatings, ensuring optical clarity and accessibility. Maintaining minimal gas and humidity leakage becomes essential, alongside ensuring a stable medium exchange protocol during the imaging process.

Secondly, the microscope system itself must demonstrate robustness to facilitate long-term time-lapse imaging. Overcoming common issues such as focus drifting is crucial while preserving high-resolution capabilities and maintaining a high level of selectivity in imaging.

Thirdly, there's a need for high-speed data acquisition capabilities and a large data storage capacity to accommodate the continuous stream of information generated during extended imaging sessions. Automatic data acquisition and processing emerge as highly advantageous for streamlining long-term imaging procedures.

Lastly, and perhaps most importantly, the choice of molecular markers for the sample holds huge significance. These markers must exhibit biocompatibility and effectively overcome the challenges of phototoxicity and photobleaching inherent in fluorophores used for long-term live-sample imaging purposes. Overcoming these hurdles is paramount to ensuring the viability and integrity of the biological samples under observation across extended imaging periods.

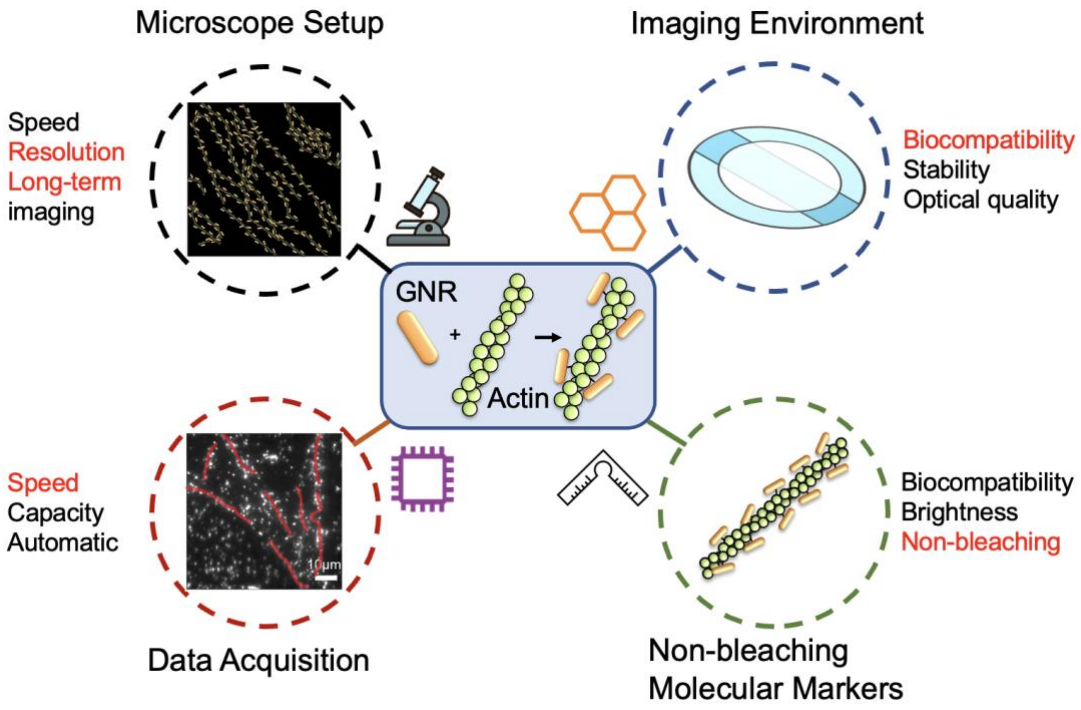

Figure 1.1: Good long-term imaging system requires proper selection and optimization of molecular marker, imaging environment, microscopy, and data acquisition.

1.3 Photobleaching and molecular markers selection

One of the primary challenges in fluorescent bio-imaging is photobleaching, which hinders continuous, long-term imaging of biomaterial or cell samples. Photobleaching occurs when a fluorophore loses its ability to fluoresce permanently due to photon-induced chemical damage and covalent modification[10]. The average number of excitation and emission cycles a specific fluorophore can undergo before photobleaching is contingent upon its molecular structure and the local environment. Once a fluorescent sample undergoes photobleaching, the fluorophores cease to be stimulated to an excited state, even when exposed to the required light energy. In Chapter 5, a demonstration was made regarding the photobleaching of a fluorophore-labeled actin protein sample, which occurred within 15 minutes (Fig. 5.3).

There are several strategies to prevent photobleaching of fluorophore-labeled samples during long-term imaging sessions. The most common approach involves reducing the intensity of excitation light while prolonging the exposure time[7]. This reduction in intensity decreases the frequency of excitation-emission cycles, thereby extending the life of fluorescent molecules. However, this adjustment may compromise the temporal resolution of imaging, creating challenges for applications such as cell segmentation and tracking. Alternatively, the application of anti-photobleaching mounting reagents can be employed to enhance photostability[11]. However, most of these reagents contain oxygen scavengers, which diminish oxygen levels in samples, potentially compromising cellular health and rendering them unsuitable for live cell imaging applications.

Hence, the selection of molecular markers for long-term bio-imaging is of utmost importance. The criterion for choosing an appropriate fluorescent marker typically includes considerations like high brightness, large stokes shift, low photobleaching tendencies, high pH stability, and biocompatibility[12,13]. On the other hand, plasmonic nanoparticles, such as gold nanoparticles, are resilient against photobleaching, making them strong contenders to replace traditional fluorescent markers. A novel method was presented involving the use of alternative bromide-free surfactants to create CTA+ free gold nanoparticles, which are not only structurally and optically stable but also biocompatible for long-term cell imaging[14]. This advancement lays the groundwork for super-resolution long-term imaging of dynamic cellular events devoid of photobleaching concerns.

1.4 Cellular environment control under in-vitro system

One of the primary methods employed for quantifying cellular and molecular behavior in single-cell imaging involves long-term in-vitro imaging systems. Notably, previous studies[9,15]

have successfully extended over substantial durations, lasting for weeks. Presently, a growing number of studies are embracing continuous in-vitro cell imaging techniques across a diverse spectrum of biological contexts from analyzing cell migration patterns[16] to shape determination mechanisms[17].

Among the various technical prerequisites for establishing a robust long-term in-vitro imaging system, maintaining the cellular environment stands out as paramount. The key point is to ensure that cells retain their physiological function and are not changed by imaging or incubation conditions[6]. However, achieving an optimal cellular environment often involves a tradeoff, as it may impact the quality of imaging[7]. Finding a balance between these factors needs careful system optimization and experimental design.

Crucial parameters such as temperature, CO_2 levels, humidity, and medium osmolality must be carefully regulated throughout the experiment. Particularly challenging is the mitigation of medium evaporation, a consistent issue in such setups. Strategies such as enclosing the entire microscope within a heated chamber help minimize temperature gradients that might cause focus drifts during imaging sessions. Alternatively, custom-designed microfluidic chips present several potential advantages including improvements in signal-to-noise ratio (SNR) by maintaining minimal volumes of culture media[18]. However, it is limited by difficulties of adaption and complexity of fabrication. Moreover, employing a small sealed on-stage incubator enhances control over gas and humidity compositions while reducing the necessary gas volumes. This approach contributes to finer control and stability within the cellular environment, ensuring optimal conditions for sustained long-term imaging studies.

1.5 Imaging system

Establishing a robust long-term imaging system contains several challenges. Firstly, the entire microscopy hardware and software infrastructure must exhibit exceptional robustness for sustained time-lapse imaging. Secondly, focus drift remains a persistent challenge, where the incorporation of a fast and efficient autofocus system could be beneficial. Thirdly, maintaining high image resolution during high-frequency imaging is challenging. Increasing the number and size of individual pixels on the CCD can enhance image resolution, sensitivity, and the area observed. Lastly, the automation of data acquisition and integration for data analysis require substantial computational efforts and rapid data retrieval capabilities.

The state-of-art bio-imaging methods achieving super-resolution predominantly utilizes spatially patterned excitation and detection of single fluorophore molecules[19–22]. Techniques like stimulated emission depletion microscopy (STED)[23], ground state depletion microscopy[24], and reversible saturable optical fluorescence transitions (RESOLFT)[25] augment resolution through the spectral separation of fluorophores displaying nonlinear responses to excitation. Others such as super-resolution optical fluctuation imaging (SOFI)[26], spectral precision distance microscopy (SPDM)[27], photoactivated localization microscopy (PALM)[28], and stochastic optical reconstruction microscopy (STORM)[29] achieve enhanced resolution by exploiting temporal separation of fluorophores. However, these super-resolution microscopy techniques rely on fluorophores prone to photobleaching, limiting the ability to visualize the cellular dynamics of over time. Moreover, the aforementioned super-resolution imaging methods, including patterned excitation and single-molecule localization approaches, often exhibit relatively slower imaging speeds (20-80 frames/sec for small field of view) and are susceptible to photobleaching limitations.

This dissertation presents a non-bleaching imaging method utilizing a plasmonic nanoscope capable of facilitating long-term imaging while achieving sub-diffraction-limit resolution.

Chapter 2 delves into the fundamentals of plasmonics, covering properties associated with gold nanoparticles, and discusses the imaging systems utilized in this project, including standard darkfield microscopy and the recently developed phase intensity nanoscopy (PINE).

Chapters 3 and 4 provide background information on the biological model central to this dissertation: the actin protein and its crucial role in cellular activities. Additionally, the neuron cell model, SH-SY5Y, is introduced along with protocols for cell line preparation in subsequent studies.

Chapter 5 addresses the traditional immunostaining fluorescent imaging method, and later comparing it with the novel plasmonic labeling method utilizing gold nanorods that discussed in Chapter 6.

Chapter 7 delves into the design and optimization of the imaging system for long-term protein and cell dynamics imaging, including chamber mechanism design and characterization of different environmental factors.

In Chapter 8, the non-bleaching imaging method is demonstrated through imaging actin cofilin disassembly and live-cell slow dynamics, followed by quantitative analysis of these activities.

Chapter 9 provides a comprehensive summary of the entire dissertation, discusses the limitations of the current work, and outlines future developments and applications.

Chapter 2 Imaging System

2.1 Plasmonics introduction

Plasmonic nanoparticles, particularly those made from noble metals, stand out among various nanoplatforms like semiconductor quantum dots, magnetic nanoparticles, and polymeric nanoparticles because of their distinct surface plasmon resonance (SPR) properties. Gold nanoparticles (GNPs), in particular, have become popular recently in biological research, especially in cell imaging applications, due to their straightforward synthesis procedures, adaptability for surface modifications, strongly enhanced and tunable optical characteristics, and excellent biocompatibility that makes them suitable for clinical applications. These GNPs can be synthesized rapidly with high quality, high yields, and precise size control, allowing the production of various shapes and structures, including gold nanorods[30–32], silica/gold nanoshells[33], and hollow gold nanoparticles[34].

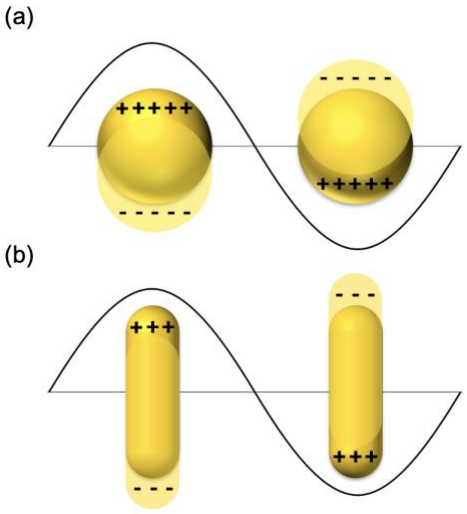

Figure 2.1: Schematic illustration of surface plasmon resonance (SPR) for (a) gold nanosphere (GNS) and (b) gold nanorod (GNR).

Plasmonic particles exhibit a property when their size is comparable to or smaller than the wavelength of the electric field, generating resonant collective coherent oscillations due to the conduction of free electrons on the metal surface (Fig. 2.1). This electron oscillation near the particle surface then induces a charge separation relative to the ionic lattice, leading to a dipole oscillation aligned with the light's electric field. This distinct behavior is termed as surface plasmon resonance (SPR). Notably, the maximum oscillation reaches its peak at a specific frequency known as the absorbance peak frequency, which can be measured using a UV-Vis spectrometer. The SPR peak wavelength can be tuned based on various nanoparticle properties, such as the metal type, particle size, shape, structure, composition, and the dielectric constant of the surrounding medium[35].

The SPR can be quantitatively explained through Maxwell's equation based on Mie theory[35]. For well separated spherical nanoparticle with radius R, the extinction cross-section C_{ext} can be expressed as[36,37]:

$$C_{ext} = \frac{24\pi^2 R^3 N \varepsilon_m^{3/2}}{\lambda} \frac{\varepsilon_i}{(\varepsilon_r + 2\varepsilon_m)^2 + \varepsilon_i^2} \tag{2.1}$$

Where N is the number of nanoparticles per unit volume, ε_m is the dielectric constant of surrounding medium, which is related to refractive index by $\varepsilon_m = n_m^2$, λ as wavelength of the incident light, ε_i and ε_r represent the imaginary and real part of the dielectric function of nanoparticle. Based on Eq. 2.1, the SPR appears when $\varepsilon_r = -2\varepsilon_m$. A notable property of gold nanoparticles is their plasmon absorption bands are in visible region, make this material suitable for many sensor applications[38].

For gold nanorod, according to Gans[39], the surface plasmon mode in small ellipsoidal nanoparticles under the dipole approximation, was anticipated to split into two separate modes, a

consequence attributed to the surface curvature and geometrical characteristics of these ellipsoidal nanoparticles. Based on Gans' theory, the extinction cross-section C_{ext} can be expressed as[36,40,41]:

$$C_{ext} = \frac{2\pi VN\varepsilon_m^{3/2}}{3\lambda}\sum_j \frac{(1-P_j^2)\varepsilon_i}{(\varepsilon_r + ((1-P_j)/P_j)\varepsilon_m)^2 + \varepsilon_i^2} \tag{2.2}$$

Where V is the volume of each particle, P_j represents the depolarization factor and e as ellipticity which are defined as:

$$P_{length} = \frac{1-e^2}{e^2}\left[\frac{1}{2e}\ln\left(\frac{1+e}{1-e}\right) - 1\right] \tag{2.3}$$

$$P_{width} = \frac{1 - P_{length}}{2} \tag{2.4}$$

$$e^2 = 1 - \left(\frac{length}{width}\right)^{-2} \tag{2.5}$$

Where the ratio of $length/width$ represents the aspect ratio of gold nanorod. Based on the Eq. 2.2, the SPR occurs when $\varepsilon_r = -((1-P_j)/P_j)\varepsilon_m$. In this scenario, there are two local plasmon resonances corresponding to longitudinal ($P_j = P_{width}$) and transverse ($P_j = P_{length}$).

Based on Eq. 2.2 and the relation between dielectric constant of gold nanorod with incident light wavelength as:

$$\varepsilon_r(\omega) = 34.66 - 0.07\lambda \tag{2.6}$$

The proportional relationship between the maximum longitudinal SPR absorption wavelength and the aspect ratio of gold nanorod can be expressed as[42]:

$$\lambda_{max} = 95(length/width) + 420 \tag{2.7}$$

Based on Eq. 2.7, the maximum SPR wavelength is linearly red shifted as the aspect ratio of gold nanorod increases. This property is very useful in the gold nanorod synthesis protocol development and validation.

Light absorption takes place as photon energy dissipates through inelastic processes. Conversely, light scattering happens when photon energy induces electron oscillations within matter, leading to the emission of photons as scattered light. This can occur at the incident light's frequency (Rayleigh scattering) or at a different frequency (Raman scattering). The oscillation of SPR enhances both light absorption and scattering by 5–6 orders of magnitude compared to the absorption capacity of most strongly absorbing organic dye molecules and the emission strength of highly fluorescent molecules, respectively[43]. The scattering light caused by nanoparticle SPR oscillation can be observed by darkfield microscopy, which is discussed in Chapter 2.2.

The ability to tune the SPR peak wavelength allows for precise control over the optical properties of plasmonic nanoparticles, enabling applications across diverse fields, from biosensing to biomedical imaging. This unique attribute of plasmonic nanoparticles, especially gold nanoparticles, has positioned them as valuable tools in advancing research and development in various scientific and medical domains[44]. To overcome the barrier between photobleaching and long-term imaging, we use gold nanorod as plasmonic label, because of the unique character of plasmonic nanoparticles as well as the polarization property[45] of gold nanorod.

2.2 Darkfield microscopy

In optical microscopy, darkfield is an illumination technique employed to enhance the signal-to-noise ratio. This method involves illuminating the sample with white light at an oblique angle while obstructing the central light beam, enabling collection of only the scattered light from the sample by the objective lens. This results in the characteristic visual effect of a dark or nearly black background against which bright objects appear[46].

Darkfield microscopy typically operates in two primary modes: transmission-mode and reflection-mode. Transmission-mode is used when the sample of interest is positioned on a

transparent substrate. In the transmission-mode setup, the condenser is positioned atop the sample stage, providing illumination from above. The darkfield condenser blocks the central beam, enabling only the peripheral beam to illuminate the sample. The objective lens situated below the sample then collects the scattered light. Conversely, reflection-mode is employed when the sample is situated on an opaque substrate.

In transmission-mode darkfield microscopy, there exist two types of condensers: dry condenser and wet condenser. A dry condenser utilizes internal optical components to generate oblique illumination. Conversely, a wet condenser directs light at a highly oblique angle at the interface between the condenser lens and air, surpassing the critical angle for total internal reflection. This necessitates immersion of the lens in a liquid with a refractive index closer to the lens, enabling the light to exit the condenser and illuminate the sample.

Gold nanoparticles, which fall below the diffraction limit of conventional optical methods, create challenges for imaging. However, these nanoparticles exhibit strong scattering intensities, as discussed in Chapter 2.1. Since scattering alters the propagation direction of light, it facilitates the spatial suppression of excitation light, enabling visualization of these particles using darkfield microscopy with enhanced contrast. Moreover, despite being smaller than the diffraction limit, the distance between nanoparticles can also be distinguished spectrally and colorimetrically using darkfield microscopy[47]. In Chapter 2.3, a recently developed nanoscopy based on darkfield, which utilizing phase intensity of gold nanorod to achieve sub-diffraction-limit resolution, is discussed.

2.3 Phase intensity nanoscopy

Here, we present a phase intensity nanoscopy (PINE) which was developed by our group and recently published[48].

A specialized multilayered film comprising polyvinyl alcohol and liquid crystalline polymers, termed the Phase-Intensity (PI) film, was developed, and fabricated to precisely regulate the phase variations between electric field components. This innovation aimed to achieve the separation of phase and intensity characteristics of nanoprobes within a restricted diffraction-limited area. The compact and slim design of the multilayer film (0.6 mm thickness) was then incorporated into a darkfield arrangement, positioned between the objective and tube lens, enabling excellent light transmission for nanoscopy.

The PI film received input light consisting of scattered light from a group of nanoprobes, specifically gold nanorods. Subsequently, this scattered light underwent a series of transformations within the PI film, wherein it was reshaped, phase-modulated, and converted from phase to intensity. The precise management of phase differences among electric field components within the diffraction-limited area allowed for the differentiation of nanoprobes from each other through phase-intensity separation. This unique capability of the PI film can be effectively represented through Jones matrices:

$$\boldsymbol{E} = \frac{1}{2}\begin{bmatrix}1 & 0\\ 0 & 0\end{bmatrix}\begin{bmatrix}e^{i\gamma/2}+e^{-i\gamma/2} & e^{i\gamma/2}-e^{-i\gamma/2}\\ e^{i\gamma/2}+e^{-i\gamma/2} & e^{i\gamma/2}-e^{-i\gamma/2}\end{bmatrix}\begin{bmatrix}e^{i\delta_x} & 0\\ 0 & e^{i\delta_y}\end{bmatrix}\begin{bmatrix}E_x\\ E_y\end{bmatrix} \tag{2.8}$$

$$\gamma = \int_0^D \frac{n_e n_0}{\sqrt{n_e^2 cos^2\theta + n_0^2 sin^2\theta}} dz - n_0 D \tag{2.9}$$

Where $\delta = \delta_y - \delta_x$ is the phase difference between electric field E_x and E_y, γ is the phase retardation, D represents layer thickness, n_0 denotes ordinary refractive index, n_e denotes extraordinary refractive index, and θ represents molecular alignment with applied electric field.

The PI was designed to contain three-layers as three different elements: a retarding element for reshaping, a variable retarding element for phase modulation, and a fixed linear polarizing element for phase-intensity conversion. The variation of intensity corresponded to phase information of gold nanorod can be then expressed as:

$$I(\gamma) = cos^2\left(\frac{\gamma}{2}\right)E_x^2 + sin^2\left(\frac{\gamma}{2}\right)E_y^2 + 2cos\left(\frac{\gamma}{2}\right)E_x sin\left(\frac{\gamma}{2}\right)E_y sin(\delta) \quad (2.10)$$

PINE demonstrated the precise determination of the spatial positions of individual gold nanorod by modulating γ from 0 to 2π radians. During this modulation, the phase difference between E_x and E_y was varied from -π to π radians, revealing the distinct positions of each nanorod.

Ultimately, the deconvolution algorithm[49] was employed to produce high-resolution images using data collected across the modulation range. For the localization of nanoprobes, a threshold was determined by computing the average of the scattering signal volume power and the noise volume power, facilitating the identification of nanoprobes. In the algorithm, each individual rod's peak positions can be represented as:

$$\begin{aligned} \mathrm{X}(Pkx, Pky) = argmin\{\left\| hX_1 + iDCT(X_2) - Yln\left(hX_1 + iDCT(X_2)\right)\right\|_1 + \lambda_1\|X_1\|_1 \\ + \lambda_2\|X_2\|_1\} \end{aligned} \quad (2.11)$$

Where h represents the point spread function, $iDCT$ denotes the inverse discrete cosine transform, Y denotes the diffraction-limited image, X_1 is the deconvolved image, X_2 is the background image, and λ_1 and λ_2 are two regularization parameters.

Given PI's displacement-free nature, the precise localization of nanoprobe populations (numbering in the thousands) creates patterns revealing complex cellular architectures, facilitating precise super-resolution imaging down to the sub-10 nm length scale. Utilizing PINE (Phase Intensity Nanoscope), we were able to quantify distributional parameters to overcome a physical limit to resolve sub-10 nm cellular architectures.

Chapter 3 Actin and Cellular Activity

3.1 Actin dynamics in cell activity

Actin, a major cytoskeleton protein, participates in many important cell activities such as cell division, vesicle and organelle movement, cell signaling and muscle contraction[50]. Over decades, researcher have observed actin dynamics through fluorophore labeling and microscopy. One disadvantage of this method is that irreversible photobleaching of fluorophores limits the time window to visualize actin dynamics to seconds to minutes. Several actin dynamics and movement have been studied in this way (Fig. 3.1), such as continuous images of single actin filament severed by cofilin over hundreds of seconds[51,52], and the dynamics involved with more filaments such as self-selective formation of streams over time[53]. However, slow dynamics such as cell division and organelle movement which cytoskeleton involved to, usually take hours and days[54]. In that case, due to the unstable property of fluorophore, the sample will suffer with photobleaching.

Actin exists in two primary forms within cells: as G-actin, a freely existing monomer recognized for its globular shape, or as F-actin, an integral component of a linear polymer. Both forms play crucial roles in essential cellular functions, including cell mobility and contraction during division. When supplied with adequate ATP and Mg^{2+}, G-actin enters an activation phase, initiating the process of polymerization.

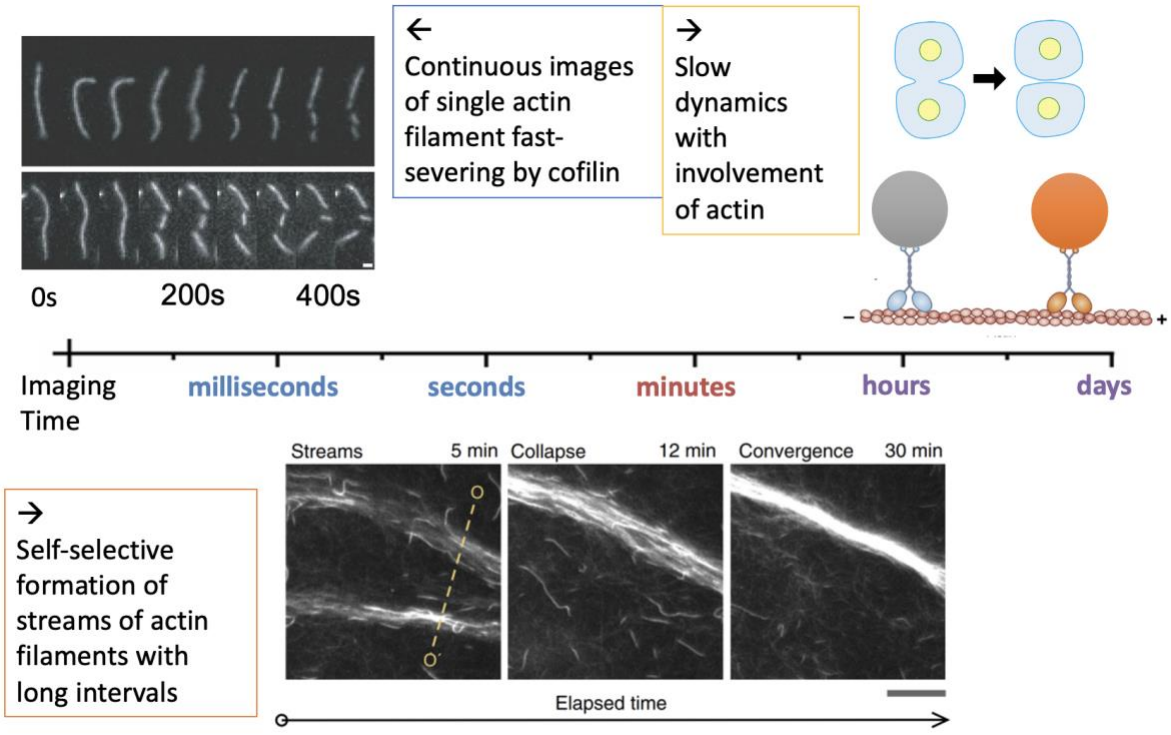

Figure 3.1: Actin dynamic events in cell activities happen across a large time scale. Events from fast to slow: Single actin filament fast-severing by cofilin[52]; Self-selective formation of streams of actin filaments with long intervals[53]; Slow dynamics with involvement of actin[54] (e.g., cell division and organelle movement).

The assembly dynamics of actin involve four distinct stages, starting with the activation phase and followed by nucleation, elongation, and a steady-state phase. During elongation, the filament undergoes rapid growth at both its pointed and barbed ends, resulting in the formation of the actin filament (F-actin), which achieves stability upon reaching a fixed total length. F-actin exhibits a double right-handed helical structure, twisting gradually around each other[55]. It is composed of repeats of 13 actin units for every 6 left-handed turns, spanning a length of 350 Å[56]. The formation of actin filaments is reversible, and their function often involves undergoing rapid polymerization and depolymerization, which enables cells to migrate. Research suggested the formation of actin filament is over two orders of magnitude more favorable at pH 6.0 than pH 8.0, and the critical concentration for polymerization is decreased at lower pH[57].

In contrast to polymers like DNA, where constituent elements are covalently bonded, actin filaments assemble through lateral bonds, contributing to their dynamic character[58]. Cofilin, an essential actin-binding protein, plays a crucial role in regulating the number of actin filaments. It achieves this by severing filaments and enhancing actin assembly dynamics, thereby increasing the available sites from which subunits can add or dissociate. When cofilin binds to a filament, it interacts with two actin-ADP molecules, inducing movement that disrupts the stability of the filament, ultimately causing it to break[55]. Recent study found that cofilin-decorated filaments have a shorter average crossover length and mean twist than native actin filaments[59]. Previous studies have demonstrated that the presence of cofilin shortens the crossover length of actin filaments from 2.2 subunits to 2.1 subunits[60]. This alteration occurs due to cofilin's influence on the twisting angle of the actin filament, prompting a rotation in the structure of actin.

There are three main groups of actin isoforms that locate in different locations with different roles. Eukaryotic organisms express different actin genes to form slightly different actin structures: α-actin located in contractile structures exclusively in muscle fibres; β-actin located in expanding edge of cells (used for mobility); γ-actin located in filament of stress fibers. Beta-actin is well-known for its involvement in cell movement: The leading edge of a mobile cell is defined by an intricate network of actin filaments. The continuous polymerization of fresh actin filaments propels the cell membrane forward, forming extensions known as lamellipodia. Moreover, β-actin is critical for cell morphology change during mitosis[61], and the disorganization of actin cytoskeleton can cause multinucleation during cytokinesis[62]. This thesis is focus on the β-actin, specifically, cell surface β-actin that facilitate cell migration and division.

3.2 Neuron cells and its character

Neurons, alternatively known as nerve cells, serve as the fundamental components of both the brain and the nervous system. They play an important role in processing sensory information from the external environment, transmitting commands to muscles, and facilitating the transformation and transmission of electrical signals at various stages. Structurally, a neuron consists of three primary components: dendrites, an axon, and a cell body. Dendrites receive synaptic inputs from axons, and the cumulative effect of these inputs determines whether the neuron will initiate an action potential. The axon serves as the neuron's output structure, transmitting electrical messages, or action potentials, throughout its length to communicate with other neurons. Additionally referred to as the soma, the cell body holds genetic information, maintains the neuron's structural integrity, and provides the energy necessary for its functions[63].

Neurons are categorized into four main types: unipolar, bipolar, multipolar, and pseudounipolar. Unipolar neurons feature a single structure extending from the soma, whereas bipolar neurons possess one axon and one dendrite emerging from the soma. Multipolar neurons are identified by the presence of one axon and multiple dendrites, while pseudounipolar neurons function as both axons and dendrites[64].

The fundamental functions of a neuron encompass receiving, integrating, and transmitting signals to target cells. Neurons communicate through synapses, where the axon terminal of one cell connects with either the dendrite or soma of another neuron, occasionally even connecting with its axon. These synapses can either increase (excitatory) or decrease (inhibitory) activity in the target neuron. Additionally, certain neurons communicate through electrical synapses, direct junctions between cells allowing electrical conduction[65].

In conclusion, understanding the role of actin during neurodevelopment and neuronal cell migration holds significant importance in neurological research and could contribute to the development of treatments for neuron disease such as Alzheimer's disease. The subsequent chapter will dive into cell line selection for the study, the differentiation of neuronal cells, and the methodology involved in preparing the cell line.

Chapter 4 Cell Line Preparation

4.1 SH-SY5Y cell expansion and differentiation

The SH-SY5Y cell line (ATCC, CRL-2266), derived from the SK-N-SH neuroblastoma cell line through three subcloning iterations, serves as a valuable model for studying neurodegenerative disorders. This cell line demonstrates versatility, as it can be induced to differentiate into diverse functional neuron types through the application of specific compounds. Widely utilized in experimental neurological research, the SH-SY5Y cell line contributes significantly to studies involving neuronal differentiation, metabolism, and functions pertinent to neurodegenerative processes, neurotoxicity, and neuroprotection.

Originally derived from the SH-SY subclone of the parental SK-N-SH human neuroblastoma cell line, established in 1970 from metastatic cells found in the bone marrow aspirate of an unknown ethnicity four-year-old female, the SH-SY5Y cell line continues to be instrumental in advancing our understanding of neurological disorders. Early studies[66–69] described the culturing conditions for undifferentiated and differentiated SH-SY5Y cell.

Here, we will discuss the purposes and methods of SH-SY5Y cell expansion and differentiation. The process of cell expansion encompasses the sequential transfer of cell populations from smaller cultures or volumes to progressively larger ones, culminating in the generation of a significant number of viable cells. The development of expansion protocols for cells intended for production or assay purposes relies significantly on certain criteria. Firstly, the cells must demonstrate phenotypic and genetic stability over successive passages, ensuring

consistent characteristics and behavior. Predictability in their behavior is crucial, signifying their responsiveness to intended stimuli or manipulations during expansion. Moreover, an essential aspect involves their capacity for seamless and efficient expansion into substantially larger volumes while maintaining high cell densities. Successful expansion strategies prioritize not only the proliferation of cells but also the preservation of their functional integrity and fidelity to their intended purpose. In this study, the cell culture expansion protocol is based on the standard neuroblastoma cell culture protocol[70] and adapted by ATCC company protocol, which is discussed in Chapter 4.2.

Neuronal differentiation is a complex process that integrates many signals to drive electrophysiological, morphological, and transcriptional changes[71]. This intricate process commences with the emergence of nascent neurites, often denoted as 'neurite outgrowth', marking the initial stages of neuronal development. Subsequently, these neurites undergo progressive evolution, culminating in the formation of a singular axon and multiple dendrites, leading to the maturation of the neuron. As this maturation proceeds, the characteristic dendritic spines also emerge, further enhancing the neuron's structural complexity and connectivity[72]. In vitro induction of neuronal differentiation can be achieved through exposure to diverse agents such as tetradecanoylphorbol acetate, brain-derived neurotrophic factor (BDNF), norepinephrine, and retinoic acid (RA)[73–75]. Specifically, RA-induced differentiation prompts the formation of neurites, whose length progressively increases over time. The majority of differentiation protocols utilized for the SH-SY5Y cell line predominantly involve RA as the sole differentiation factor, typically spanning a few days[76,77]. Post this differentiation period, cells are primarily characterized based on morphology. The differentiation of SH-SY5Y cells holds paramount importance in our study. Through the application of plasmonic labeling (discussed in Chapter 6), one can delve into the

cellular actin activity that contributes to morphological changes and signaling dynamics during the differentiation process. The cell differentiation protocol is based on and adapted the standard differentiation protocol[78], which is discussed in Chapter 4.3.

4.2 SH-SY5Y cell expansion

The SH-SY5Y cell expansion was executed through a multi-passage process which could be separated into three phases：

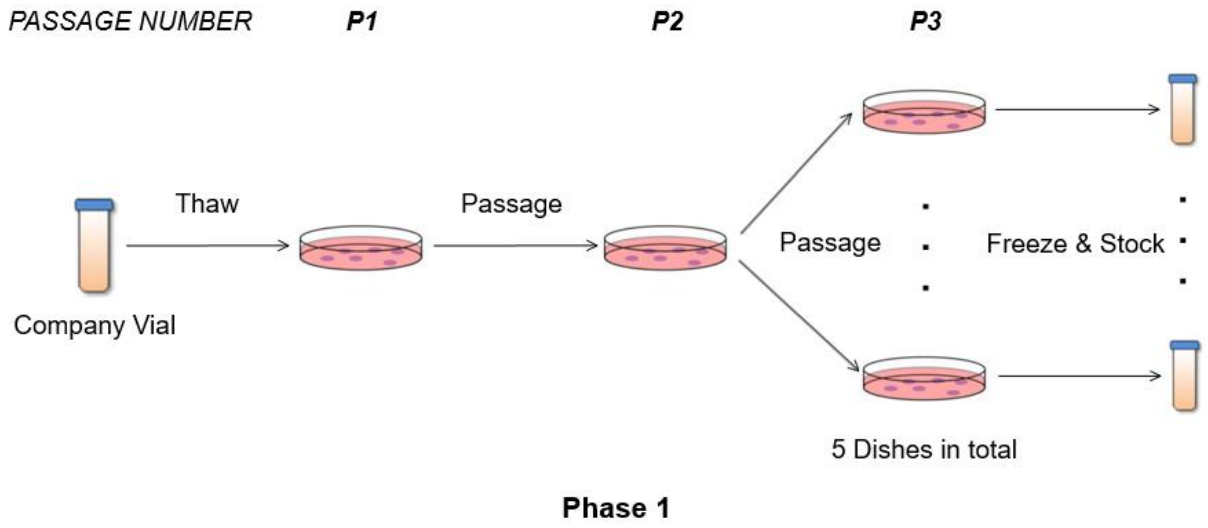

Figure 4.1: Phase 1 of SH-SY5Y cell expansion includes three passaging rounds and one freezing and stock round.

In phase 1 (Fig. 4.1), the source cell was firstly thawed down and transferred to a single dish, cultured regularly following the cell culture procedure that suits SH-SY5Y. For the standard environment, we used 37°C and 5% CO_2 with DMEM, 10% FBS and 1% Penicillin-Streptomycin (Penstrep) as the culture medium. Then cell was split into five different dishes through passaging. Cell coverage of large or equal to 70% would be suitable for passage. During each passaging, cells were firstly washed by PBS 3 times and treated with Trypsin-EDTA for 3 minutes under standard environment. After detachment, the cell pellets were collected and centrifuged down at 2000x rpm

for 3 minutes. The cell pellets were then resuspended with cell culture media after removal of Trypsin-EDTA and split equally to five different dishes. Each of the dishes were split equally into another five dishes following the exact same procedure as described above. At this point, the passage number of each dish is 3, and we labeled them as the 1st generation (GA1 – GE5) which would be 25 in total.

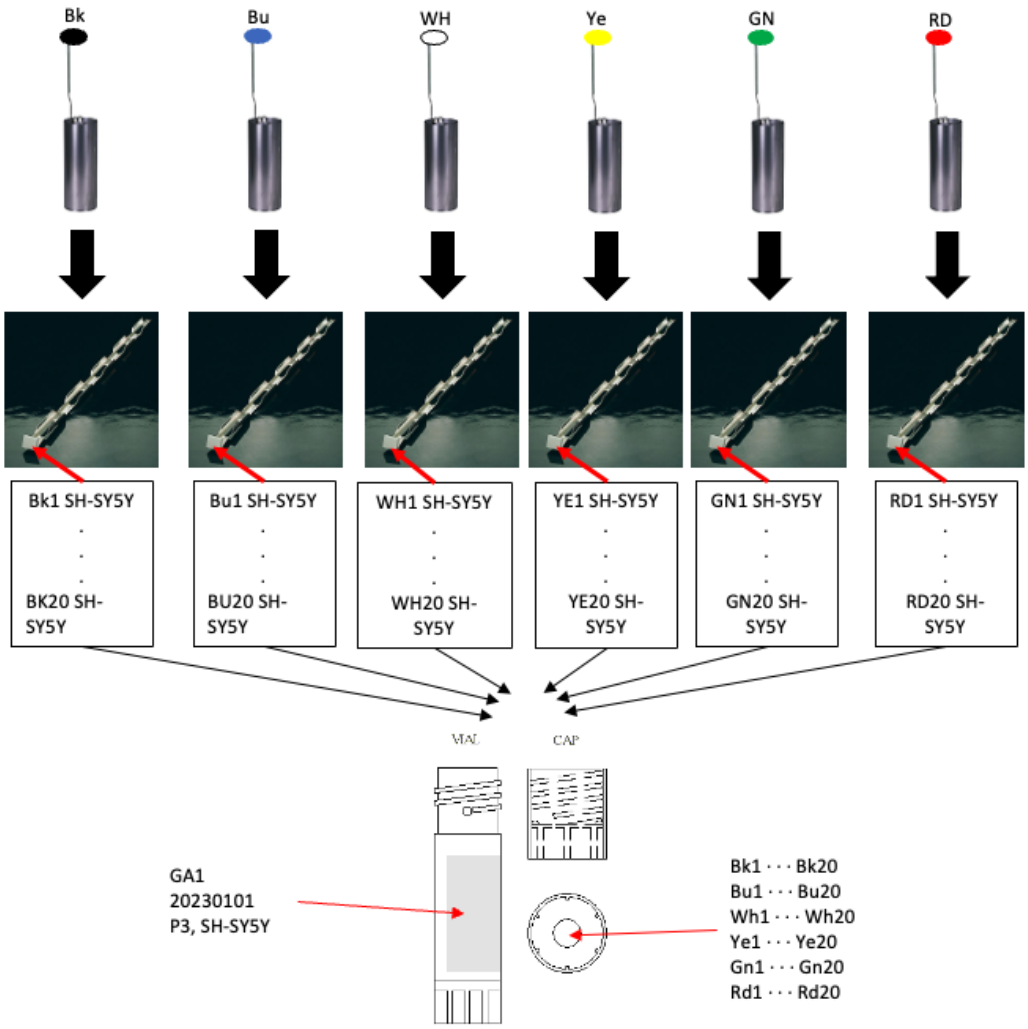

Figure 4.2: Cryo storage and labeling example for generation GA1 (P3) SH-SY5Y cell.

First-generation cells were frozen and stocked following the standard cryo storage procedure for longer storage purpose. In terms of cell freezing, trypsinization and hemocytometer

cell counting were done prior to transferring cells with freezing media (90% FBS + 10% DMSO) into cryo vials and then slowly cooled down to -80°C through freezing container. After 24 hours, cryo vials were transferred to the liquid nitrogen tank with proper labeling (Fig. 4.2).

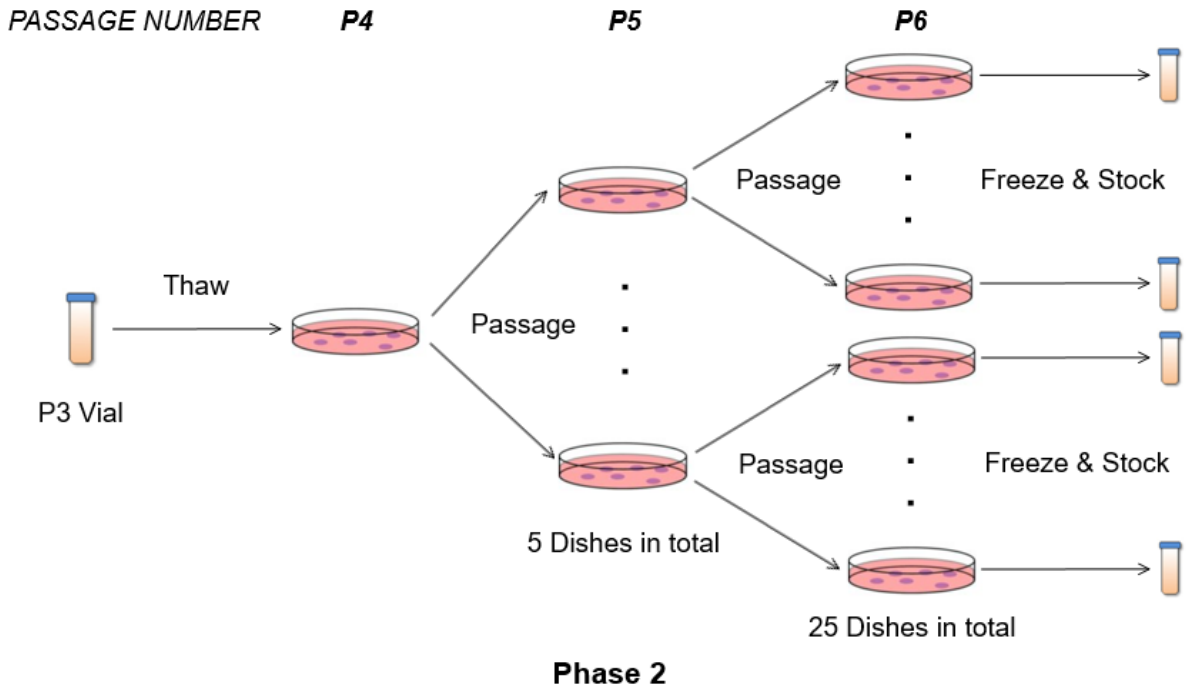

Figure 4.3: Phase 2 of SH-SY5Y cell expansion includes two passaging rounds and one freezing and stock round.

In phase 2 (Fig. 4.3), one of the first-generation cells prepared in phase 1 was thaw down from liquid nitrogen storage and further expanded. During the thawing down process, SH-SY5Y cell was transferred from cryo vial by washing with warmed media and centrifuged down at 1500x rpm for 5 minutes to remove DMSO. The cell pellets were then introduced to a new dish and followed the same passaging process described in phase 1 to expanded to 25 dishes. At this point, the passage number of each dish is 6, and we labeled them as the 2nd generation. As an example of using GA1 for 1st generation seed, the 2nd generation would be GA1A1 – GA1E5 which would be

25 in total. Second generation cells were also frozen and stocked in liquid nitrogen for longer storage purpose.

The 2nd generation cell was regularly cultured following the standard culture protocol until reaches 25th passage. This period is called phase 3 (Fig. 4.4) and the cell samples used in the experiments discussed in this dissertation were all from this phase.

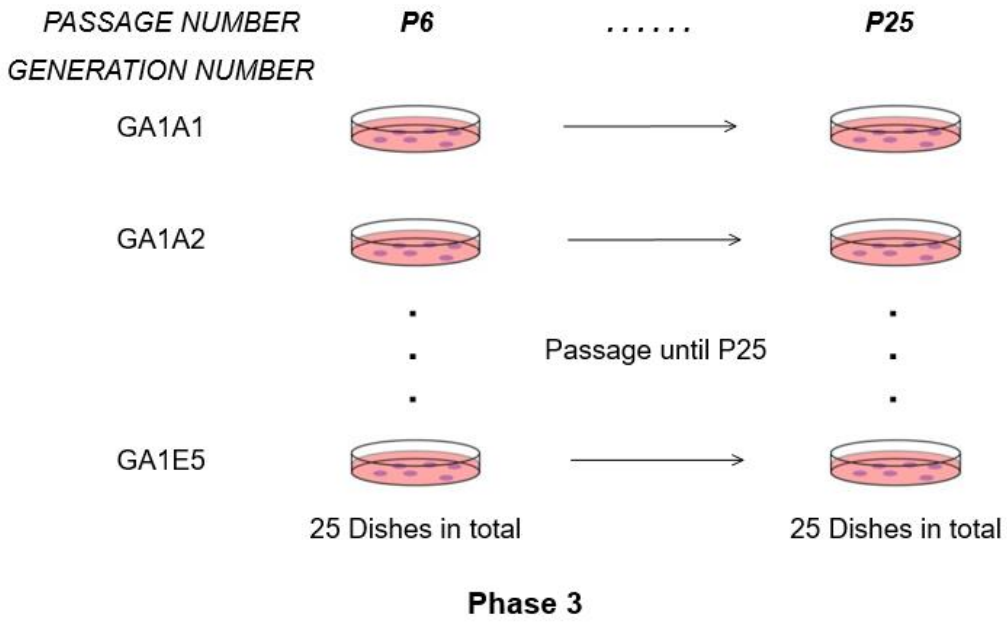

Figure 4.4: Phase 3 of SH-SY5Y cell expansion includes 19 rounds of passaging until the cell passage number reaches 25.

4.3 SH-SY5Y cell differentiation

The SH-SY5Y differentiation is the process by which human neuroblastoma cell line SH-SY5Y is differentiated, or specialized, into human dopaminergic neurons (Fig. 4.5). The differentiation is a multi-day process in which neurons could be obtained from primary cells (SH-SY5Y).

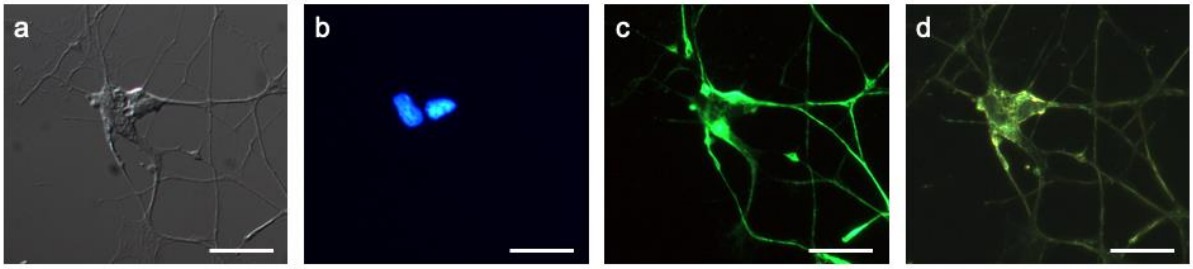

Figure 4.5: Images of differentiated neurons from human neuroblastoma cell line, SH-SY5Y. Neuroblastoma was differentiated using a combination of 10 μM retinoic acid (RA), extracellular matrix, and brain-derived neurotrophic factor (BDNF). (a) Image of neurons taken using differential interference contrast (DIC) microscopy. (b) Image of two nuclei by DAPI immunostaining. (c) Image of cytoskeleton of neurons by anti-neurofilament (NF) immunostaining. (d) Image of neurons taken using darkfield microscopy. All images were taken at 400x magnification. Scale bar: 10 μm.

The primary cells (SH-SY5Y, < 15 passages) were firstly cultured in regular media (DMEM, 10% FBS and 1% Penstrep) until reaching 70% coverage prior to the seeding. Then, cells were seeded in a MaxGel ECM pre-coated dish with differentiation media (DMEM, 10% heat-inactivated FBS, 1% Penstrep, 2 mM L-Glutamine and 50 μM Retinoic Acid) under 10,000 cells/cm^2 seeding density. Differentiated SH-SY5Y cells to day 5 with regularly changing differentiation media until cells were differentiated into neurons in which most neurites have length larger than 100 μm. Next, neuronal media (Neurobasal Media, 2% B-27, 1% Penstrep, 2 mM GlutaMAX, 20 mM KCl, 50 ng/mL BDNF and 2 mM db-cAMP) was exchanged with old media in order to further develop and extend neurites. After day 7 the cells could be considered fully differentiated (Fig. 4.6) and the neurons could be maintained for 14 days with changing neuronal media regularly. The fixation, staining of differentiated SH-SY5Y and DIC microscopy methods are discussed in the following method sections. The fluorescent imaging method is discussed in Chapter 5.2.

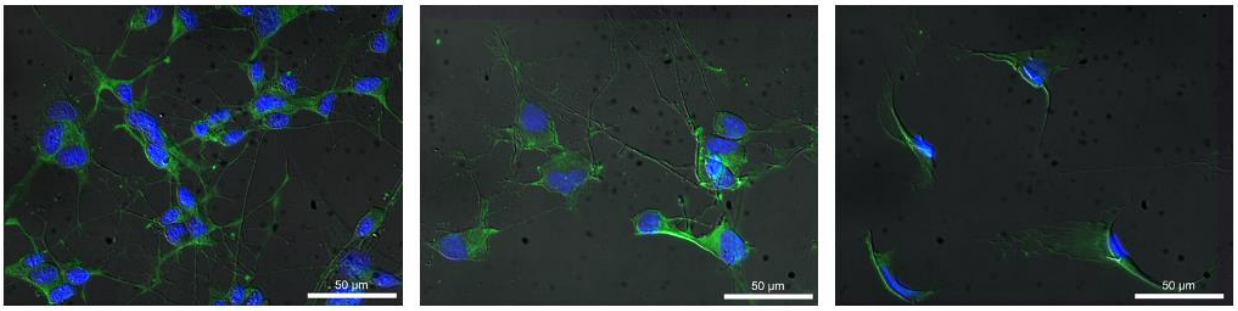

Figure 4.6: Merged differentiated SH-SY5Y (day 11) images of DIC (cell and background), FITC (actin filament) and DAPI (nucleus). Scale bar: 50 µm.

In conclusion, the SH-SY5Y cell line was chosen as the model for this study due to its versatility and capacity for differentiation. The expansion of the SH-SY5Y cell line was accomplished through a three-phase freezing-thawing cycle, resulting in the availability of 25 2nd generation cells. The differentiation of neuronal cells was demonstrated using both differential interference contrast (DIC) microscopy and immunostaining. This provides an opportunity to explore actin activities during the gradual and intricate process of neuron maturation.

Cell fixation and staining method:

Firstly, 15 mm round glass slides were placed in a 35 mm petri dish before seeding the SH-SY5Y cell. Cells went through the multi-day differentiation procedure that described previously until neurons were fully developed. The sample were then washed, treated with 4% paraformaldehyde for 35 min and washed again. After fixation, cells were permeabilized with 0.5% Triton X-100 in DPBS for 2 min, followed by 30 min washing. Next, cells were blocked with 5% goat serum in PBS for 1 hour, followed by 30 min washing. After blocking, cells were treated with 1% Monoclonal Anti-Neurofilament in 1% BSA solution in DPBS for 1 hour, followed by 30 min washing. Then, cells were treated with 1% Goat anti-Mouse IgG (H+L) Secondary Antibody Alexa 488 in DPBS for 1 hour, followed by 30 min washing. After antibody treatment, sample was mounted by Fluoroshield Mounting Medium for 5 min. Finally, glass slides

that contain cells were retreated from dishes and sealed with another glass slide. The stained cell sample can be preserved at room temperature until imaging by fluorescent microscopy. All washing procedures were operated with DPBS.

DIC microscopy method:

Differential interference contrast (DIC) microscopy, alternatively known as Nomarski interference contrast (NIC) or Nomarski microscopy, represents an optical imaging method employed to heighten contrast in transparent, unstained samples. DIC operates based on interferometry principles, unveiling details in specimens that would otherwise remain unseen. Its intricate optical setup generates an image where the subject appears in varying shades of grey against a neutral background. DIC functions by splitting a polarized light source into two mutually coherent components with orthogonal polarization. These parts are spatially shifted (sheared) at the sample plane before being recombined for observation. The resulting interference between these components at recombination is sensitive to disparities in their optical path lengths (i.e., the product of refractive index and geometric path length). As these rays traverse different regions of the sample separated by the shear, any variance in refractive index or thickness prompts distinct optical path lengths. Consequently, one ray undergoes a phase alteration concerning the other due to delays incurred by propagation through materials with varying optical densities.

All the DIC image acquisitions were performed on IX-73 (Olympus, inverted) microscope. A halogen light (Olympus, U-LH100-3-7), after a frosted glass filter and a quarter wave plate, worked as the light source (white light) to illuminate the sample. A linear polarizer was inserted between microscope light port and Condenser Wollaston (Olympus, IX-LWPO) to produce the necessary plane-polarized light for interference. The incident wavefronts of plane-polarized light were split into mutually perpendicular polarized components by the Wollaston prism. The

polarized light from sample was then pass through objective lens (Olympus, UPLFLN40X; Olympus, LUCPLFLN60XPH) and then to the objective Nomarski prism (Olympus, U-DICTS) to recombine the sheared wavefronts in the conjugate plane. The interference DIC image was finally collected with a color CCD camera (Q-Imaging Regita 3000).

Chapter 5 Fluorescent Actin Labeling and Imaging

5.1 Actin filament preparation

Figure 5.1 shows the principle for the standard fluorescent labeling method of actin filament. The primary antibody will first bind to the target protein, and then introducing 2nd antibody that is pre-conjugated with fluorophore (e.g., Alexa Fluor 488). The 2nd antibody will target specifically to the primary antibody and will eventually label the whole actin filament with fluorophore.

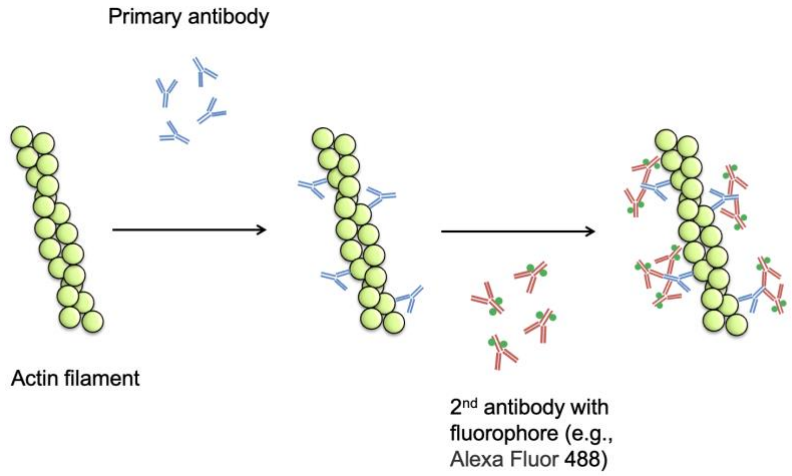

Figure 5.1: Principle of standard fluorescent labeling method of actin filament.

Fluorescent actin labeling method:

Before the experiment, 1 mg lyophilized unlabeled G-actin protein were reconstituted to 10 mg/mL with DI water; 200 μg lyophilized fluorophore (Alexa Fluor 488) labeled G-actin protein were reconstituted to 2 mg/mL stocking solution by addition of 0.5 mL 2 mM Tris-HCl, pH 8.0. Then, the concentrated labeled and unlabeled actin protein were both diluted to 1 mg/mL

working solution by adding 1x actin storage buffer (2 mM Tris-HCl at pH 8.0, 200 μM ATP at pH 7.0, 500 μM TCEP at pH 7.0, 0.1 mM $CaCl_2$) and stored in -30°C.

For fluorescent F-actin polymerization, 1.29 μL of 1 mg/mL unlabeled G-actin, 1 μL of 1 mg/mL fluorophore labeled G-actin, 15.71 μL of 1x actin storage buffer and 2 μL of 10x KMEI buffer (500 mM KCl, 100 mM HEPES-KOH, 10 mM EDTA, 10 mM $MgCl_2$, pH 7.0) were mixed and incubated in dark and at room temperature for 1 hour to polymerize F-actin. To visualize F-actin under fluorescent microscope, 5 μL of 0.1% methylcellulose was firstly spread on the center of a 24 mm*30 mm microscope cover glass and dried. Then, 2 μL F-actin solution was dropped on the center, covered with another 15 mm round cover slide and sealed. The sample was stored in the dark and monitored with a fluorescent microscope.

Our result shows that freshly prepared F-actin filaments (Fig. 5.2 (a)) turned to have shorter average length and less twisting, while aged F-actin filaments (Fig. 5.2 (b)) had longer length and more twisting between each other. That verified the actin polymerization and aging mechanism discussed in the recent published paper[79].

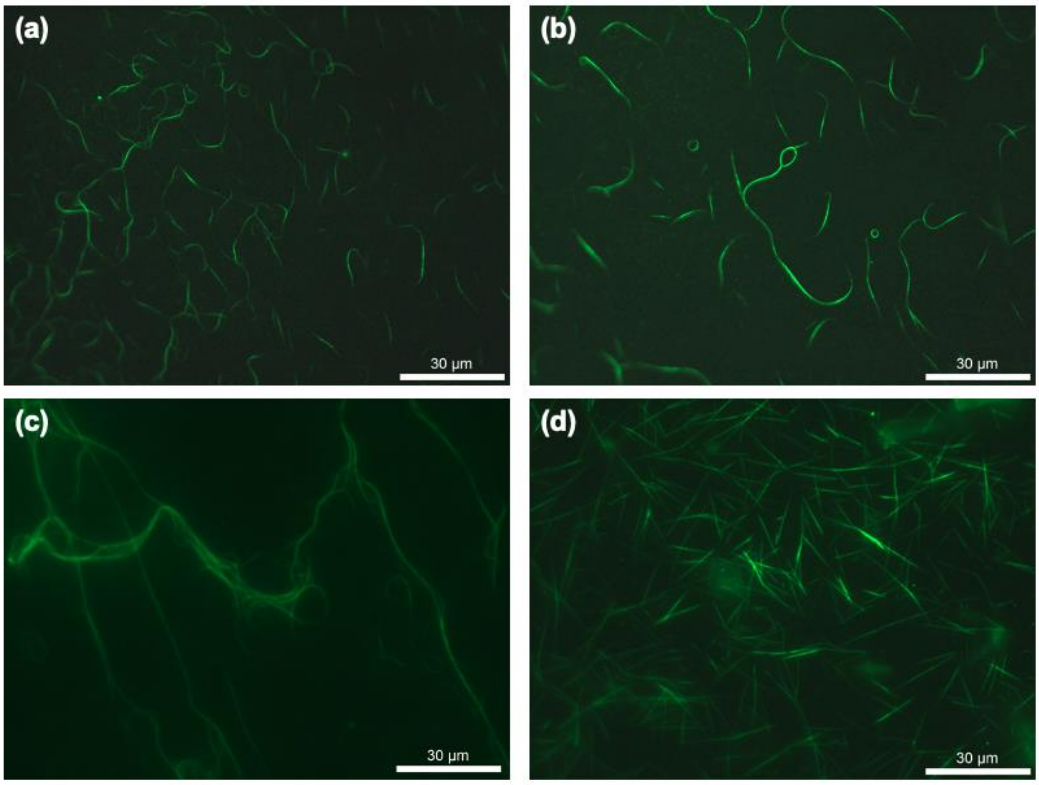

Figure 5.2: Fluorescent F-actin filament and actin bundle. (a) Freshly prepared F-actin filament. (b) Aged F-actin filament (day3). (c) Alpha-actinin actin bundle. (d) Fascin actin bundle. Scale bar: 30 μm.

5.2 Actin bundle preparation

Actin bundle is the structure that actin filaments are crosslinked through actin binding protein and forming three-dimensional network that constitute majority of cytoskeleton. In this case, we utilized two actin binding proteins (alpha-actinin and fascin) to demonstrate the photobleaching for traditional fluorescent protein imaging.

To bundle the F-actin, fluorescent F-actin filaments were firstly prepared following the polymerization procedures described in Chapter 5.1. Then, 400 nM actin binding protein (alpha-actinin or fascin) was introduced to the F-actin solution and incubated for another 15 minutes in the dark. To visualize F-actin bundle under the fluorescent microscope, 5 µL of 0.1%

methylcellulose was firstly spread on the center of a 24 mm*30 mm microscope cover glass and dried. Then, 3 μL F-actin bundle solution was dropped on the center, covered with another 15 mm round cover slide and sealed. The sample was stored in the dark and monitored with a fluorescent microscope.

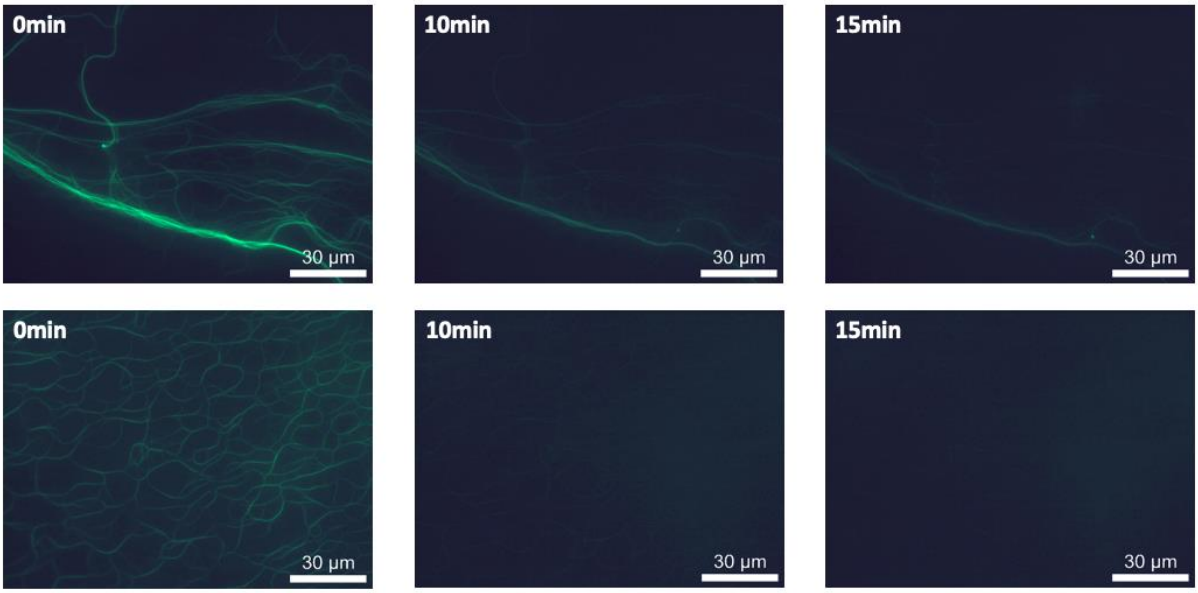

Figure 5.3: Fluorescent F-actin filaments under photobleaching. Scale bar: 30 μm.

With the presence of alpha-actinin (Fig. 5.2 (c)), actin network was further extended and tangled compared with aged actin. With the presence of fascin (Fig. 5.2 (d)), actin network turned to be short, straight and more crossing with each other.

The major disadvantage of fluorescent protein labeling and imaging, photobleaching, was also demonstrated. Two forms of actin (F-actin filament and alpha-actinin actin network) were labeled with fluorophore (Alexa Fluor 488) and tested under fluorescent microscope (FITC channel): Firstly, F-actin filaments were totally photobleached in 10 to 15 minutes (Fig. 5.3). Aged and self-bundled actin filament (by methylcellulose) could have slightly longer photobleaching time (Fig. 5.3 top row). Secondly, actin binding protein can slow down the photobleaching process

by combining multiple filaments and forming network. With addition of alpha-actinin, in which photobleach surpasses depolymerization, the alpha-actinin actin network can still be distinguished after 40 minutes, with loss of image quality (Fig. 5.4).

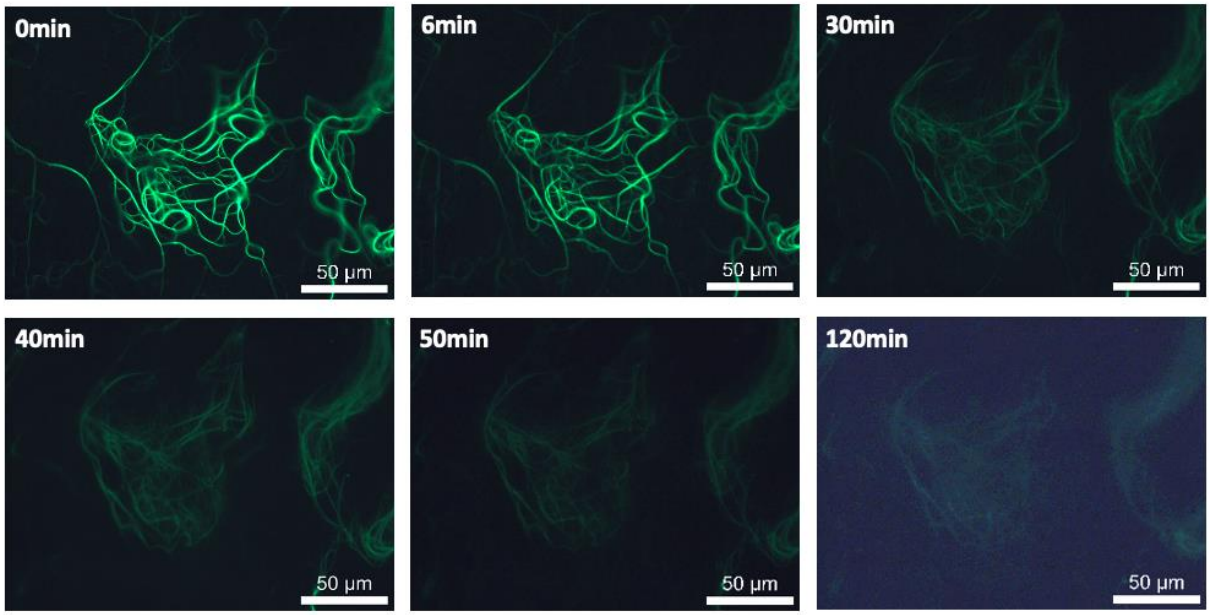

Figure 5.4: Fluorescent Alpha-actinin actin network under photobleaching. Scale bar: 50 µm.

In conclusion, the standard immunostaining method using fluorophore as the molecular marker was discussed and demonstrated using standard fluorescent microscopy. Notably, photobleaching was observed on both actin filament and alpha-actinin actin bundle samples within 30 minutes.

Fluorescent imaging method:

All the fluorescent image acquisitions were performed on IX-73 (Olympus, inverted) microscope. Illumination light was a fluorescence light source (Olympus U-HGLG-PS) with a spectrum from 340 nm to 780 nm, which was then filtered by specific filter cube/mirror unit for specific staining dye, and then excited fluorophore to illuminate the sample. The light from the light source was firstly passed through the excitation filter (bandpass filter) to restrict the

illumination wavelength. A dichroic mirror was used to reflect illumination light to the objective lens (Olympus UPLFLN40X N1478600; Olympus UPLFLN100X OI2-2) and focus the light to the sample plane to excite the fluorophore. The emitted light from the fluorophore was then passed through the objective lens and then emission filter (bandpass filter) located in each fluorescent filter cube to eliminate the excitation light, only allowing emitted light to pass through. Filter cubes for DAPI (excitation filter: 347-60 nm, dichroic mirror: 409 nm, emission filter: 447-60 nm) and FITC (excitation filter: 475-35 nm, dichroic mirror: 520 nm, emission filter: 499-43 nm) were selected and used for actin filament imaging (FITC) in Chapter 5 and for stained cell imaging (FITC, DAPI) in Chapter 4 and Chapter 6. Finally, the emitted fluorescent signal was collected with a color CCD camera (Q-Imaging Regita 3000). For fluorescent actin imaging in Chapter 6, a b/w CCD camera (Hamamatsu Orca II) was used to collect the images.

Chapter 6 Plasmonic Actin Labeling and Imaging

6.1 Plasmonic labeling

To overcome the barrier between photobleaching and long-term imaging, we use the unique character of plasmonics and purpose a labeling method based on that. Plasmonic particles, for example gold nanoparticles, if their size is under or comparable to the electric field wavelength, will generate a resonant oscillation (SPR) due to the conduction of electrons on its surface[44]. The absorbance peak wavelength can be tuned by controlling the size of gold nanoparticles[38]. In this work, I used gold nanorod as plasmonic label. Using the polarized property of gold nanorod, a new non-bleaching nanoscale imaging method on target protein, followed by quantitative analysis on actin protein network were demonstrated.

To demonstrate the quantitative method over long-term nanoscale imaging, the Actin-Gold Nanorod (GNR) network was firstly obtained. The Actin-GNR network was created through several steps including gold nanorod synthesis, gold nanorod ligand exchange, and actin plasmonic labeling. The detailed procedures and results are discussed in the rest of this chapter.

6.2 Gold nanorod synthesis and ligand exchange

Gold nanorods with average size 80 nm*30 nm were synthesized by seed-mediated method with bromide-free surfactants as previously reported recipe[80]. In summary, the seed solution was prepared by mixing 5 mL of 0.5 mM $HAuCl_4$ with 5 mL of 0.2 M CTAB solution and followed by injecting 0.6 mL of 0.01 M $NaBH_4$ under vigorous stirring. The seed solution was then aged for 30 min. The growth solution was prepared by dissolving 6.15 g of CTAC and 1.234 g of NaOL

in 250 mL of DI water. The solution was then mixed with 18 mL of 4 mM $AgNO_3$ and 250 mL 1 mM $HAuCl_4$. Waiting until the solution became colorless, 5 mL of HCl (37 wt. % in water, 12.1 M) was added. After 15 minutes, 1.25 mL of 0.064 M ascorbic acid was added and followed by mixing with 0.8 mL of previously prepared seed solution. After 30 seconds of stirring, the solution was then left undisturbed at 30°C for 12 hours to allow growth. The obtained growth solution was then washed by centrifuging and resuspending in DI water twice to remove the surfactant. The synthesized gold nanorods were stored at room temperature for further usage.

The synthesized gold nanorods were ligand exchanged by modifying a round-trip phase transfer method to replace CTAC to PEG[81,82]. 0.5 mL of $3.5x10^{-8}$ M CTAC-capped gold nanorods were firstly mixed with 1 mL of 1-Dodecanethiol (DDT) and 1.5 mL of acetone. The mixture was gently swirled for 2 minutes to facilitate the first phase transfer, in which the CTAC-capped gold nanorods become DDT-capped gold nanorods and were subsequently extracted from the aqueous phase to the organic phase.

Next, the organic phase solution with gold nanorods was added with 1 mL of toluene and 5 mL of methanol. The mixture was then spun down by centrifuging with 6500 RCF for 8 min. The gold nanorods were then resuspended in 1 mL of toluene by 30 second of sonication. The gold nanorods solution was then added into 9 mL of 0.1 M 6-mercaptohexanoic acid (MHA) toluene solution at 95°C and was stirred at 1150 RPM for 15 minutes. During the reaction, visible black pellets were formed, and the solution color changes from black to transparent. After 15 minutes, the pellets were washed twice with toluene and once with isopropyl alcohol (IPA). Following washing, 3 mL of DPBS was added to the black pellets to re-suspend the gold nanorods. The gold nanorods solution was then centrifuged down and incubated in 3 mL of 1 mM PEG solution, which is a mixture of 90% of methoxy PEG thiol and 10% thiol PEG acetic acid. The PEG solution was

then gently swirled at 200 RPM for 48 hours. The PEG-capped gold nanorods were stored at 4°C for further usage.

6.3 Actin filament plasmonic labeling

Now that the rods have been stripped of CTAC and are coated in PEG, our aim is to introduce a suitable cross-linker to facilitate the attachment of proteins to these modified rods. To accomplish this, we require a strategic approach that will create a connection from the functional group on the PEGylated rods (specifically, the carboxyl group) to another functional group present on our target protein. Most proteins contain Lysine residues, which feature primary amines, providing an ideal target for our cross-linking strategy using an NHS-ester.

The process involves a reaction illustrated in Fig. 6.1: initially, N-(3-Dimethylaminopropyl)-N-ethylcarbodiimide hydrochloride (EDC) reacts with the carboxylic group to generate an O-acylisourea intermediate. Subsequently, this intermediate undergoes nucleophilic attack from the amine, resulting in the formation of an amide bond, or it might undergo hydrolysis, regenerating the carboxylic group. To enhance the stability of the intermediate and overall efficiency of the linking process, N-Hydroxysulfosuccinimide sodium salt (Sulfo-NHS) is included. Sulfo-NHS couples with EDC, forming an NHS ester, which is notably more stable than the O-acylisourea intermediate and leads to increased linking efficiency[83].

The effect of EDC concentration on actin gold nanorod crosslinking was tested (Appendix Fig. A.1 (a)) and quantified (Appendix Fig. A.2 (a)). With low EDC concentration, most of EDC were hydrolyzed during functionalization, yield to very low functionalized GNR and poor labeling quality. Crosslinking operated best with 25 mM – 50 mM EDC concentration. With this certain amount of EDC, most of GNRs were functionalized properly and could act as crosslinkers for F-actin. Well labeled actin could be seen under darkfield with red/yellow color, while red color

indicates less carboxylic (–COOH) groups on single GNR were functionalized. When EDC concentration went higher, all –COOH groups on single GNR were functionalized before crosslinking with actin. F-actin filaments turned to crosslink with only a small number of GNRs, forming bright aggregations. In this case, instead of "GNRs outlined F-actin network", we saw small regions of bright aggregation, which contained high dense F-actin around several GNRs. In addition, the labeling quality under EDC concentration can also be represented by average crosslinker distance of Actin-GNR network (Appendix Fig. A.2 (a)). Similar to mesh size[84], the crosslinker distance is defined as the distance between crossed points of a network[85], which we used as an indicator of Actin-GNR aggregation. A more spread-out and mesh-like network will have a higher average crosslinker distance. More detailed method and analysis are discussed in Appendix A.

The successfully labeled Actin-GNR network could be preserved in sandwich made with glass slides to observe under darkfield in long term. The plasmonic probe (gold nanorod) captured the same shape and contour of actin network, compared with traditional fluorophore labeling method (Fig. 6.2). With introduction of gold nanorods, the labeled network was closer to the actin bundle than single actin filaments. A reasonable guess is single functionalized gold nanorod should have multiple active ester groups which will eventually form amide bonds with both G-actin monomers on the same filament and on the different filament. In such case, functionalized gold nanorods act as the similar role as actin binding proteins (alpha-actinin and fascin), which bundle multiple filaments together and form a network.

Practically, we utilized crowding agent like methylcellulose (MC) to help forming the Actin-GNR network during crosslinking. Methylcellulose is a bulk-forming laxative that derived from cellulose, which is widely used as crowding agent in protein immobilization as it can adjust

solution's viscosity. The effect of MC concentration on actin gold nanorod crosslinking was tested (Appendix Fig. A.1 (b)) and quantified (Appendix Fig. A.2 (b)). In the morphology standpoint, a higher concentration of MC prevented actin filament aggregation and reduced the thickness of the bundle, yielded a more spread-out Actin-GNR network. The average crosslinker distance also showed slow increase with higher MC concentration, while the loose network had high crosslinker distance with absence of MC. More detailed method and analysis are discussed in Appendix A.

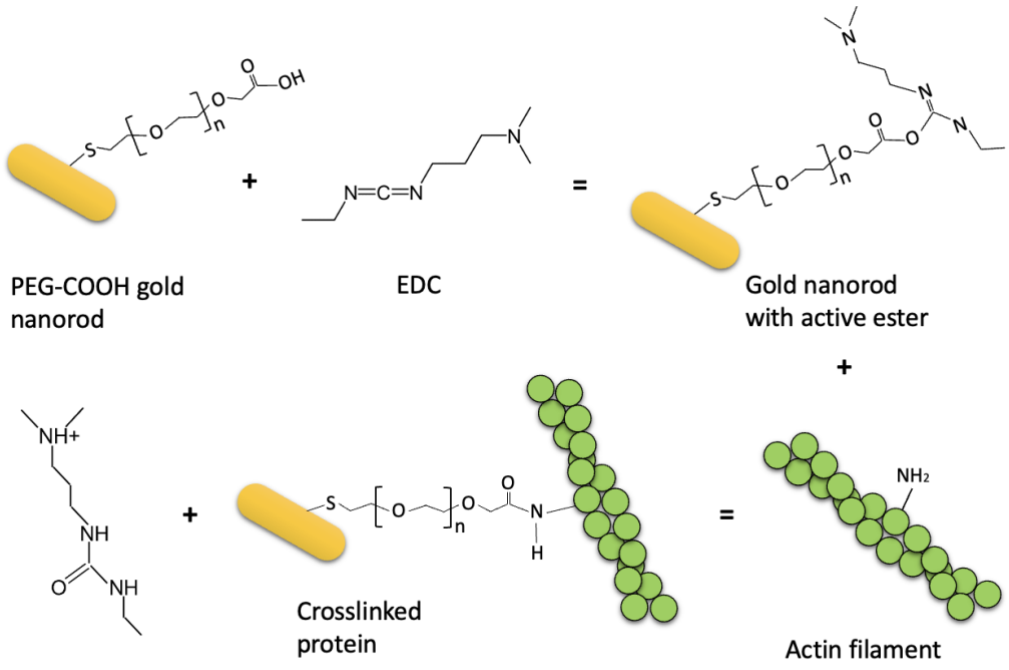

Figure 6.1: Principle of actin filament crosslinked with gold nanorod.

Gold nanorod actin conjugation crosslinking method:

Actin polymerization (solution A): To prepare the actin polymerization buffer, the actin polymerization buffer was made by dissolving 50 mM KCl, 10 mM HEPES, 1 mM EDTA, 1 mM $MgCl_2$, 0.2 mM ATP, 0.1 mM $CaCl_2$ into de-ionized water (KMEI buffer) and then titrated to pH 7.5 with 0.05 M Na_2HPO_4 and HCl. The polymerization was performed from 1 µL unlabeled G-

actin (1 mg/mL) and 18 μL of pH 7.5 KMEI buffer for 1 hour. 1 μL biotin-phalloidin was added to reduce actin filaments depolymerization.

Gold nanorods functionalization (solution B): The synthesis, purification and ligand exchange of gold nanorods were performed following Chapter 6.2. The ligand exchanged gold nanorods (80 nm*30 nm, OD (optical density) = 40, absorption peak = 732 nm) were concentrated to absorbance 18, which was measured by a UV-Vis spectrometer. For functionalization, 0.19 mg of EDC, 0.54 mg of Sulfo-NHS into 17 μL of pH 6.0 KMEI buffer (titrated by 50 mM MES and NaOH) made up the reaction buffer. Then, 3 μL of gold nanorods solution was added into the reaction solution (make the final concentration of EDC 50 mM, Sulfo-NHS 125mM). Let the solution react for 20 minutes and 1 μL (18 nM) of 2-mercaptoethanol was then added to quench the functionalization for another 10 minutes. The quenching step is designed to prevent actin aggregation from excess crosslinking within amino acid. After quenching, the functionalized gold nanorods solution is ready to use for crosslinking purposes.

Crosslinking: solution A and solution B were mixed at the volume ratio 1:1 for 1 hour at 4°C right after the functionalization procedure. A practical volume/concentration for one reaction could be 10 μL 1 nM for both F-actin and gold nanorods. For imaging purposes, 20 μL of 0.1% methylcellulose was firstly spread on the center of a 24 mm*60 mm microscope cover glass and then dried. Then, 6 μL gold nanorod labeled F-actin solution was dropped on the center, covered with another 24 mm*30 mm cover slide, and sealed to avoid evaporation during the long-term imaging. The sample was stored at room temperature and monitored under darkfield microscopy.

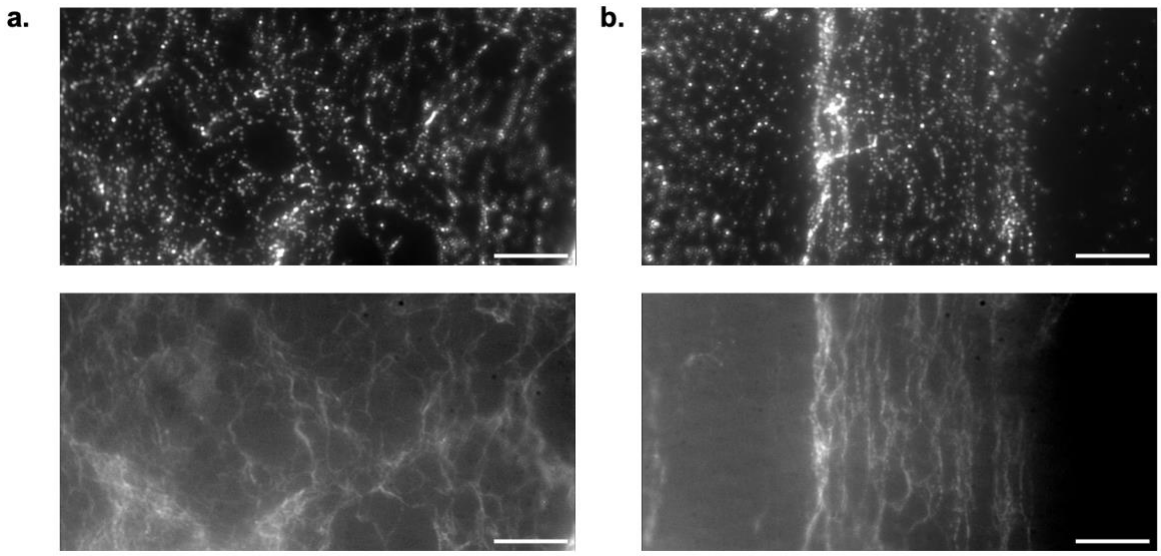

Figure 6.2: (a) (b) Actin filament labeled with gold nanorod (top image) and labeled with fluorophore (bottom image). Scale bar: 20 μm.

6.4 Cellular actin plasmonic labeling

The crosslinking method described in 6.3 could be broadly used in single protein labeling. However, cell surface contains different kinds of protein that could all be crosslinked with functionalized gold nanorods. Therefore, different from bulk actin filament/bundle labeling, in order to maintain specific labeling on the cell surface actin (β-actin), we adapted the crosslinking method with additional steps of actin antibody conjugation. The detailed method is discussed as follows and the results are shown in Fig. 6.6.

Gold nanorod cell surface actin conjugation by actin antibody method:

The ligand exchanged PEG-Carboxyl gold nanorods (96 nm*36 nm, OD = 40, absorption peak = 695 nm) were firstly prepared and aliquot in a volume of 50 μL. Then, the rods were mixed with a 8 μL EDC solution (10 mg/mL in 100 mM MES buffer, pH 5.0) and a 12 μL Sulfo-NHS solution (10 mg/mL in 100 mM MES buffer, pH 5.0), and incubated at room temperature for 45

minutes. After conjugation, the rods were washed 4 times by centrifugation at 6500 RPM for 20 minutes. Each time centrifugation was completed, the supernatant was decanted, and an equal volume of DI water was added. After first washing, the rods were incubated with 8 μL 200 μg/mL β-actin antibody (c4) at room temperature for 90 minutes while gentle rotating. Next, rods were washed again 2 times by centrifugation at 5500 RPM for 13 minutes. At the final wash, after supernatant was decanted, the rods were then resuspended in DPBS to create a 50 μL solution. The actin antibody functionalized gold nanorods can be preserved under 4°C for several months until cell labeling.

In terms of cell surface actin labeling, the cell culture chamber was firstly fabricated by attaching a self-designed PDMS well (25 mm*25 mm*5 mm) on a glass microscope cover slide (60 mm*24 mm). Next, SH-SY5Y cells were seeded and cultured in the chamber for several days to reach the proper density (~100,000 cells/cm^2). The sample were then washed, treated with 4% paraformaldehyde for 5 min and washed again. After fixation, cells were blocked with 1.5% BSA solution in DPBS for 30 minutes, followed by 3 times washing. After blocking, cells were treated with actin antibody functionalized gold nanorods (prepared ahead of time following the procedures in Chapter 6.3) in 1.5% BSA solution in DPBS (gold nanorod to 1.5% BSA ratio = 1:3) for 1 hour, followed by 3 times washing. After gold nanorod labeling, the sample was mounted by Fluoroshield Mounting Medium for 5 min. Finally, the PDMS well was removed, and sample was sealed with another glass cover slide. The cell sample can be preserved at room temperature until imaging. All washing procedures were operated with DPBS.

6.5 Nanoscale Actin-GNR Imaging and Analysis

To achieve the sub-micro resolution, we proposed a super-resolution image reconstruction algorithm using the polarization property of the GNR marker. In addition, the unique property

could also be used in network quantification that would indicate the physical distribution of plasmonic labeling on actin. The Actin-GNR network images were taken under thirty-four different polarization states, twenty degrees apart from each state. Then through deconvolution algorithm, we were able to get a reconstructed image only revealing the locations of each gold nanorod. Detailed procedure of darkfield imaging and image processing are discussed in the method section in the end of Chapter 6.5. The reconstructed image (Fig. 6.3 (a)) showed the shape of actin network itself with sub-micro resolution.

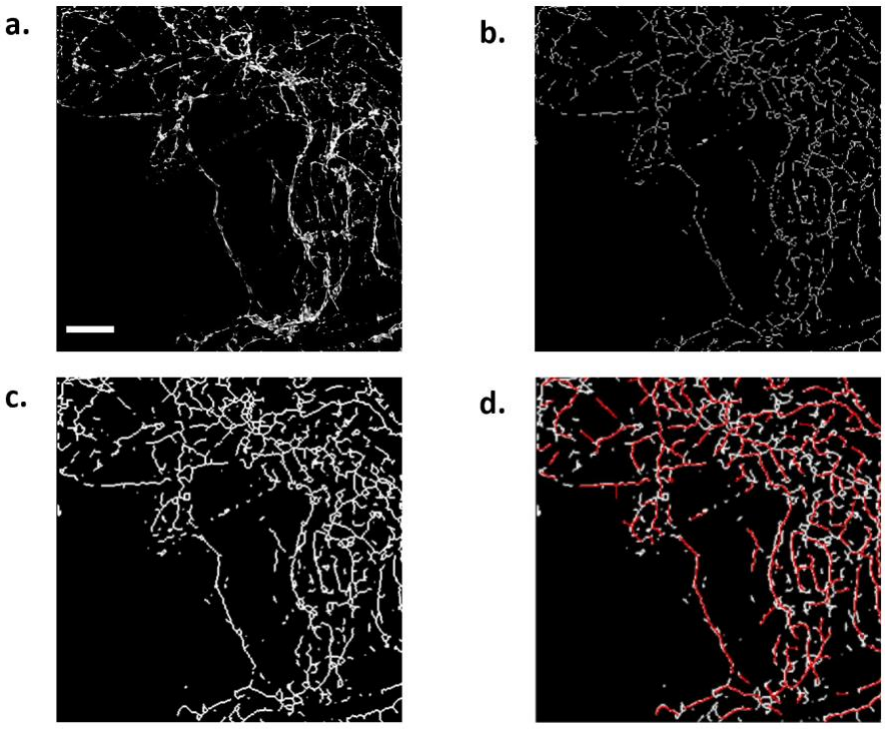

Figure 6.3: Image reconstruction and post-processing steps including visibility enhancement and ridge detection help extracting quantitative information from actin network. (a) Actin network polarized image by darkfield microscopy. (b) Skeleton map was generated based on the polarization information of gold nanorods; filaments are condensed down into single pixel thick lines with neighboring pixels. (c) Reconstructed and visibility-enhanced skeleton map. (d) Ridge detection was applied to extracted quantitative information of actin filaments and small structures. Scale bar: 10 μm.

The acquired Actin-GNR network data then went through post-processing in order to achieve better visualization and quantitative analysis. Based on the polarization information, we

were able to generate an angle map (Fig. 6.4 (b)) of the crosslinked network on top of the reconstructed image. The network image then converted to a skeleton map (Fig. 6.3 (b)) where the filaments are condensed down into single pixel thickness lines with a pre-designed number of neighboring pixels. The skeleton map was then reconstructed by further adding a certain shape (square or diamond) of neighboring pixels around the original pixel for better visibility (Fig. 6.3 (c)). The discontinued error of the skeleton caused by conversion was also fixed based on GNR angle information. Finally, ridge detection (Fig. 6.3 (d)) was applied to detect actin filaments and small network structures for further quantification.

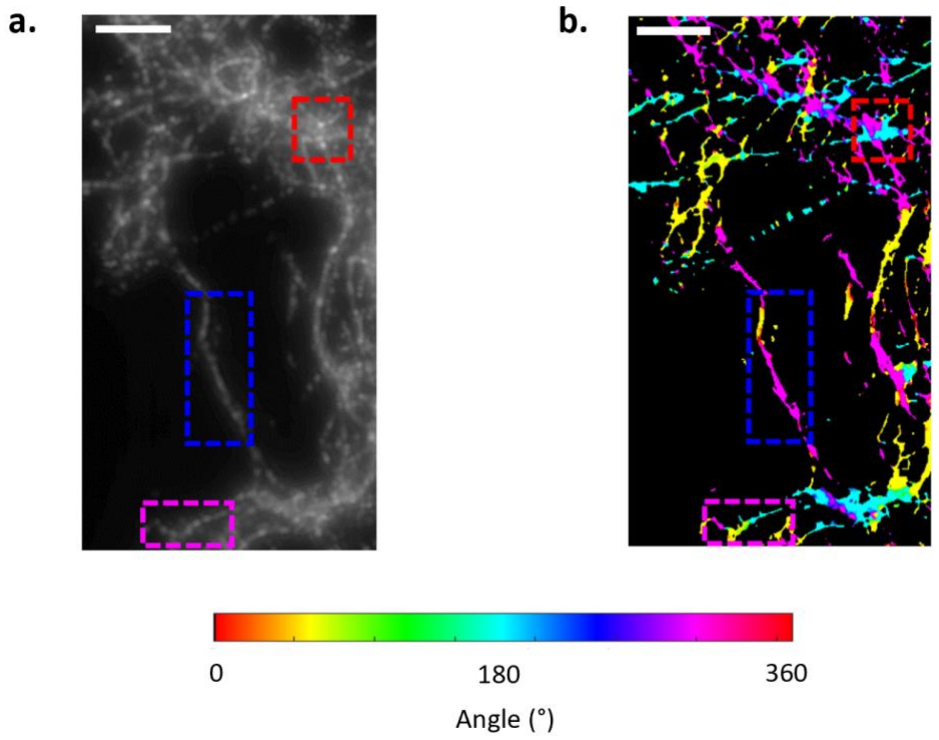

Figure 6.4: Actin structure was visualized and quantified via angular map generated based on polarization information of plasmonic label. (a) Diffraction-limited darkfield actin network image. (b) Actin network angular map. As shown in the three regions (red, blue, pink), the data indicate gold nanorods have parallel orientation with most of the actin filament structures. Scale bar: 10 μm.

From the angle map (Fig. 6.4 (b)), one can find a unique character of the GNR labeling from the corresponding network structures. For the "I – shape" network structure (blue dash line), gold nanorods orientation remained in a small range, and mostly in parallel with the actin filament. For the "Y – shape" (pink dash line) and "star – shape" (red dash line) network structures, the orientation angles of gold nanorods distributed more widely. This is because the GNR turns to have the same orientation of the actin filament it binds. We also verify our hypothesis through SEM later. This character of GNR binding could lead to interesting applications such as structure characterization. For example, different shape of Actin-GNR network structure will lead to different angular distribution, and we are able to use them for quantification. I further characterized the angle distributions (Fig. 6.5 (b-d)) of the three standard shaped network structures discussed above. Based on the angle distribution, we can further classify network structures in the future, and fast-identify the complexity of the network.

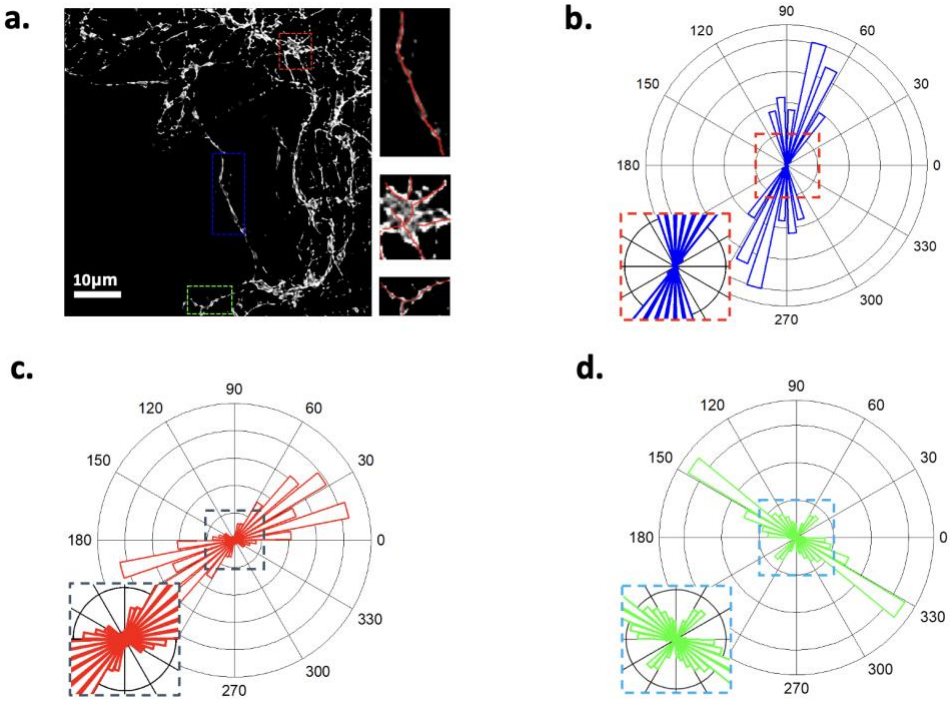

Figure 6.5: Actin network structure was quantified via angular map. (a) Three different types of actin network structures detected by post-processing. (b)(c)(d) The angle distributions of three different types

of actin network structures marked by blue box, red box, and green box in (a) respectively. That verifies previous observation of gold nanorods turned to label as the same orientation as actin filaments. Scale bar: 10 μm.

After verification the plasmonic labeling method with protein and the demonstration that we are able to do non-bleaching nanoimaging (Chapter 6.3), we introduced the same labeling method to cells. The gold nanorods (96 nm*36 nm) were firstly coated with actin antibody that targets β-actin on cell surface (Fig. 6.6 (a), (b)). Then the functionalized GNRs were introduced to SH-SY5Y cells and labeling the cell (Fig. 6.6 (e), (i)). The procedures of GNR functionalization and cell staining are illustrated in Chapter 6.4 and Chapter 4.3 respectively. Compared with control samples (Fig. 6.6 (c), (d)), the functionalized GNRs had a very good selectivity, and achieved high labeling efficiency and quality. Finally, background substruction algorithm[86] was applied to the polarized images (Fig. 6.6 (g), (k)) in order to remove unpolarized components from the images, in this case, the scattering light of cells. Based on the background subtracted images (Fig. 6.6 (h), (l)), it would be feasible to apply the quantification method we discussed above and analysis the protein dynamics during live cell activities.

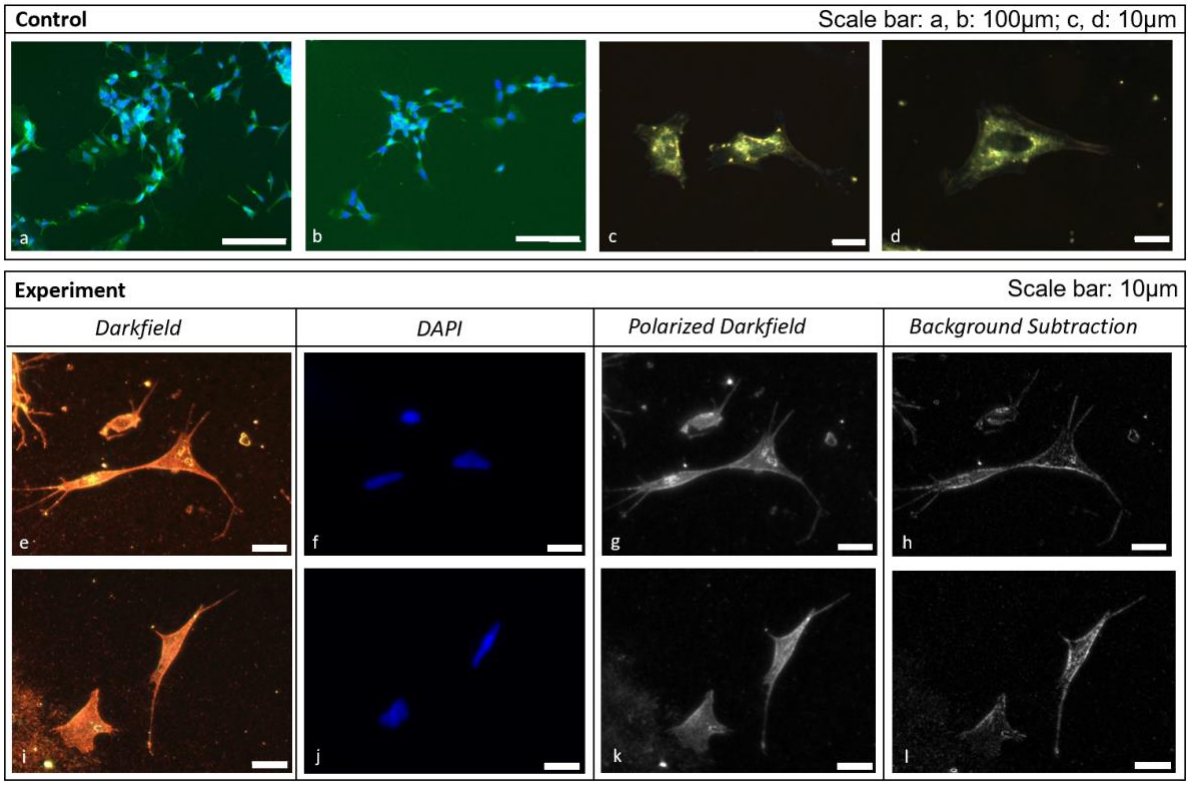

Figure 6.6: Nanoprobe labeled actin visualized through polarized darkfield imaging. (a)(b) Antibody β-actin labeling through immunofluorescence staining. (c)(d) The control samples indicated the non-specific binding between unfunctionalized rods and cells were eliminated. (e)(i) Darkfield images of antibody-coated gold nanorods labeled SH-SY5Y surface β-actin. (f)(j) Nucleus labeled by DAPI. (g)(k) Darkfield images after applied polarizer to remove unpolarized components and scattering light. (h)(l) After applying background subtraction algorithm. Scale bar: 100 μm and 10 μm.

In conclusion, we proposed and demonstrated a novel plasmonic labeling method utilizing actin as the target protein and gold nanorods as the markers. The method involved several steps, including gold nanorod synthesis, ligand exchange, functionalization, and actin conjugation crosslinking. Through the plasmonic labeling method, the plasmonic probe (gold nanorods) accurately captured the shape and contour of the actin network with high labeling density and quality. Subsequently, non-bleaching nanoscale imaging and quantification, such as the angular distribution of gold nanorods on the actin network structure, were successfully achieved. Furthermore, we also demonstrated the identification of extracellular β-actin on the cell surface

using the proposed labeling method, which providing a unique opportunity to observe protein dynamics during live cell activities. This plasmonic labeling and quantification method can be extended to other protein-nanoparticle hybrid materials, thereby facilitating their broader applications.

Darkfield imaging and image reconstruction method:

All the darkfield image acquisitions were performed on IX-73 (Olympus, inverted) microscope. A halogen light (Schott, KL 2500 LCD), after a frosted glass filter and a quarter wave plate, worked as the light source (white light) to illuminate the sample. A glycerol immersed darkfield condenser (Olympus, U-DCW) was used to couple the objective lens (NA 0.75, 40x, Olympus, UPLFLN40X N1478600) for darkfield imaging. The scattered light from the sample was firstly pass through IVM (self-designed voltage-tunable Imaging Variable Modulator)[87] and then collected with a CCD camera (Hamamatsu, Orca II) at the left-side camera port, between which two positive lenses were inserted to create a 4f system to expand the diameter of incident beam.

Sample (gold nanorods labeled actin filaments or cells) was placed on the stage. A heating system was attached to the darkfield condenser to keep the temperature constant at 37°C. While imaging, 34 steps voltage signals were sent from LabView software (National Instruments) on the computer through a DAQ card (National Instrument, 16-Bit, 8-Channel, 1 MS/s PXI Analog Output Module) and connector block (National Instrument, BNC 2110) to IVM which adjusted the axis of the polarization state on the arrival of the edges of voltage signals. The connector block, at the same time, sent the trigger signals to the CCD to externally trigger the image acquisitions of each polarization state. The exposure time was set to 306.6 ms and gain factor 0. The brightness

of the light source and position of the shutter were adjusted to avoid any over-exposure points on the image before capturing.

Image processing: the imaging processing was performed in MATLAB (MathWorks). The algorithm was adapted from FISTA (fast iterative shrinkage thresholding algorithm)[49], and the penalty parameter was set at [0.12 1], iteration time 10,000 for each frame.

Firstly, the precise positions of gold nanorods were localized by analyzing the diffraction limited images with the PSF of single gold nanorods in FISTA. Then 34 frames of images were combined together to make up the reconstructed image. A nonlinear curve-fitting function was then applied to fit the data with cosine square function. For further analysis, the final image was interpolated using a Modified Akima cubic Hermite interpolation at the factor of 5, and fake color (mpl-inferno) was added in ImageJ after remapping the brightness of the image to 0-65535.

Chapter 7 Imaging System Optimization

7.1 Actin flow chamber characterization and optimization

So far, we have discussed the imaging system for static protein or cell imaging with high resolution. To further achieve long-term continuous imaging for protein and cell dynamics, a platform is needed to provide a stable condition for both sample and imaging. Here in this chapter, we will discuss the design and optimization of the imaging system for long-term protein and cell dynamics imaging.

First, I focus on the actin flow chamber, the chamber designed to serve as the viewing platform for actin dynamics. The major requirement for this chamber is to mount the actin filament with high intensity bonding since buffer solution will be introduced as the carrier of the protein. The mechanism of binding actin to the chamber needs to be easy to deploy and not affect the natural form and behavior of actin filament. Moreover, we want the secured actin filaments to form a 2-D layer in the flow chamber. A multi-layer or 3-D network of actin would cause difficulties in the imaging and post image processing. For example, it was hard to locate the focal plane when the network is thick when under high magnification. The configuration of the chamber is also essential to this application, including the open/sealed design, the channel shape and dimension, which will affect flow type and flow rate.

For the recent few decades, researchers have applied different approaches on observing actin and actin dynamics. The key method employed to examine the actin dynamics by actin binding protein in a controlled environment is the pyrene actin assembly assay. This assay utilizes the environmentally sensitive fluorophore pyrene, which serves as an indicator of the

polymerization status of actin[88]. Pyrene-labeled actin integrated into a filament emits notably stronger fluorescence compared to a labeled monomer in a solution. To observe actin dynamics such as assembly and disassembly, one widely used technique is staining polymerization reactions with fluorescently labeled phalloidin and utilizing fluorescence microscopy[89]. The process of fixing actin with labeled phalloidin represents a direct and uncomplicated approach that can be concurrently conducted with fluorophore labeled actin experiments.

Phalloidin is a common protein that is used for actin mounting due to its high affinity binding with F-actin and selectively binding. Phalloidin not only binds with F-actin with high affinity, it can only bind to F-actin (filament) but not G-actin (monomer). Phalloidin binds specifically at the interface between F-actin subunits, locking adjacent subunits together.

Table 7.1 summarizes some key characters of imaging system used in various actin dynamics imaging applications. Noted that all the labeling methods listed in the table are using fluorophore, which mostly fall into Alexa 488 (FITC)[90] or tetramethylrhodamine (TRITC)[91]. The fluorophore was either pre-labeled with G-actin before polymerization or pre-crosslinked with phalloidin and then binding to F-actin directly. Although by using microscopy such as total internal reflection fluorophore (TIRF)[92] or epifluorescence microscopy[52], they could achieve high resolution with fluorophore labeling, but the actin dynamics time window is limited from hundreds of seconds to tens of minutes[53]. Regarding the flow chamber, there are two major types of configurations, open setup[93] and closed (sealed) setup. Both configurations are based on glass slide, and most of them select a media to separate the two glass slides to create a flow channel. The channel serves as the viewing chamber for the actin dynamics, and its height could be controlled by stacking media (tapes, parafilm, etc.)[94,95].

The mounting mechanism differs based on the platform configuration, and their research objectives. Some of the papers utilize silanization and PEGylation to coat actin binding protein to mount actin filament to the surface[90]. Silanization is a common process to create a self-assembled monolayer on glass surface by forming lateral siloxane (Si-O-Si)[96]. The process includes hydroxylation step to create a hydrophilic surface on glass slide, and APTES (3-Amino propyl tri ethoxy silane) treatment step to form the silanols groups (Si-O-H) and amine groups ($-NH_2$). PEGylation refers to the attachment of polyethylene glycol (PEG) polymer chains on glass surface. PEGylation reduces non-specific binding between actin and glass slide, which creates single actin filament resolution. Actin binding proteins such as heavy meromyosin (HMM)[95] and filamin[97] are commonly used to create specific binding between actin to surface. In addition, crowding agent is another popular additive to slow down the flow rate and facilitate the formation of actin filament network[98].

Reference	Mounting mechanism	Platform configuration	Actin label
Claessens, 2006[93]	Silanization	Open setup droplet	TRITC
Kueh, 2008[97]	Actin binding protein (filamin)	Perfusion channel separated by parafilm	Alexa 488 and 647
Schaller, 2010[95]	Actin binding protein (heavy meromyosin) + crowding agent (nitrocellulose)	Flow chamber sealed by vacuum grease	Alexa 488
Lieleg, 2011[91]	Glutaraldehyde	Stress-controlled rheometer	TRITC
Hansen, 2013[90]	Silanization and crowding agent (methylcellulose)	Flow cell separated by tapes	Alexa 488
Iwase, 2017[53] Robaszkiewicz, 2020[94]	Actin binding protein (heavy meromyosin) + crowding agent (methylcellulose)	Flow cell separated by tapes	TRITC
Wisanpitayakorn, 2017[98]	Crowding agent (nitrocellulose)	Glass slides sandwich	Alexa 488

Table 7.1: Comparison of mounting mechanism, platform configuration, and labeling method of various actin imaging technologies.

Here, an actin flow chamber setup (Fig. 7.1) is presented to utilize gold nanorod (GNR) as plasmonic label for actin filament. The two glass slides were separated with a certain gap to create a channel large enough for labeled actin and actin binding protein to flow. The gap was adjusted to 200 μm for the optimized volume and the shape of the chamber was designed to be a rhombus shape (Fig. 7.2 (f)) for laminar flow. Instead of mounting the actin on the substrate, we mount the actin on the top surface, which is more suitable for darkfield imaging and prevents light from traveling through the channel, thus enhances the imaging quality. The mounting method utilized silanization and PEGylation, to create specific bonds between phalloidin and pre-labeled actin filament. The phalloidin was pre-secured through biotin-neutravidin layer, where density can be engineered by controlling the mPEG to Biotin-PEG ratio. The ratio was optimized to 9:1 for the best mounting quality. After the Actin-GNR network formation on the top surface, we then introduced binding protein (cofilin) through the flow. The whole platform was set on an inverted darkfield microscope stage for long-term imaging. A similar chamber system setup has also been used in single particle surface CRISPR-Cas conjugation application[99] by our group. Detailed procedures of the setup are discussed in Chapter 7.2. Actin cofilin dynamics result and analysis are discussed in Chapter 8.

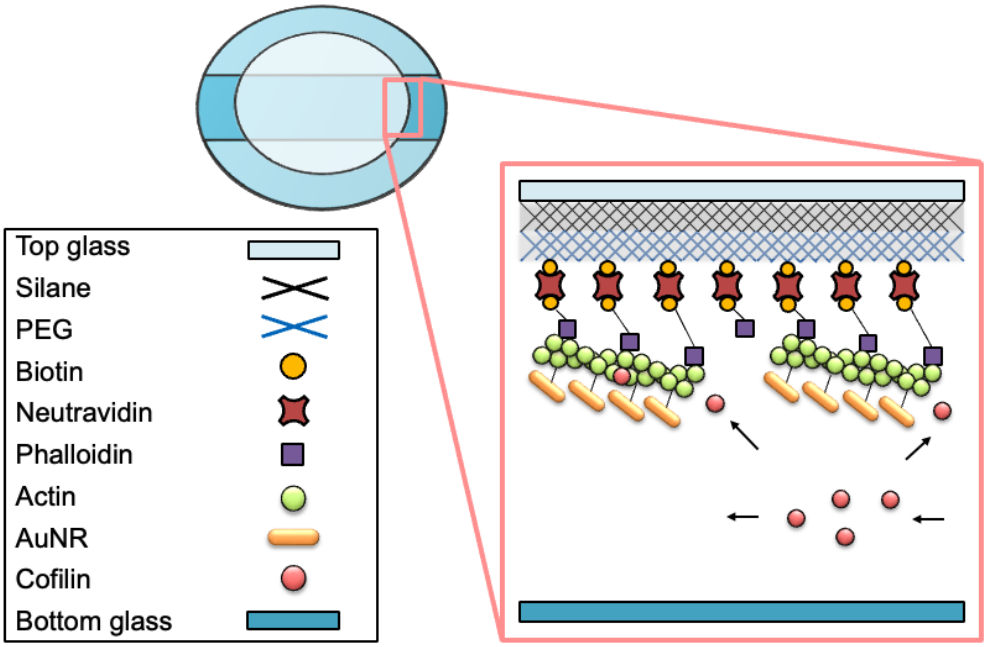

Figure 7.1: Actin flow chamber design. Layers from top to bottom: top glass, silane coating, 9:1 mPEG:Biotin-PEG coating, Neutravidin, Phalloidin, Actin-GNR network, cofilin (actin binding protein), bottom glass.

7.2 Actin flow chamber assembly, coating, and imaging setup

Here, I will discuss the necessary steps to setup the actin flow chamber prior to the long-term imaging. First, the flow chamber was assembled and properly coated following the mounting mechanism principle described in Chapter 7.1 and chamber setup design in Fig. 7.1. Then, actin filaments were mounted and then labeled with GNRs in the chamber. Finally, the chamber was transferred to the imaging stage and connected to a syringe pumping system. Detailed procedures of each step are discussed in the following method sections.

Actin Flow chamber assembly and coating method:

One 30 mm round glass slide was pre-cleaned by soap, DI water, submerging in acetone for 30 min and washed by ethanol. Next, one side of 30 mm glass slide was uniformly plasma treated for 30 seconds (Fig. 7.2 (a)) and coated 24 hours with sufficient APTES-Ethanol (standard

ratio 1:32 or higher) solution. Then, the glass slide was cleaned by ethanol followed by coating 24 hours with 9:1 PEG solution (example of 0.5 mL: 22.5 mg of mPEG-5000-NHS and 2.5 mg Biotin-PEG5000-NHS mixed with 0.5 mL of 0.1 M Sodium Bicarbonate solution) (Fig. 7.2 (b)). The PEGylated glass slide was cleaned by DI water and dried completely (Fig. 7.2 (c), (d)). Finally, to assemble the flow chamber, another pre-cleaned 40 mm round glass slide was introduced as the bottom substrate. A flow channel (length*width*height in mm: 2.5*1.5*0.2) was created in the center of the bottom glass by double-side tapes (Fig. 7.2 (e)). The PEGylated surface was faced down, served as the top of the channel. The sealed configuration (Fig. 7.2 (f)) was developed to prevent evaporation of the buffer from both inlet and outlet. To set it up, two short capillary tubing (.010" ID) were inserted into the gap of the flow chamber as inlet and outlet. A rhombus shape was created by glue to seal the chamber completely and maintain laminar flow during the experiment (Fig. 7.7). The sealed setup flow chamber was firstly primed by syringe to remove all bubbles prior the experiment (Fig. 7.2 (g)).

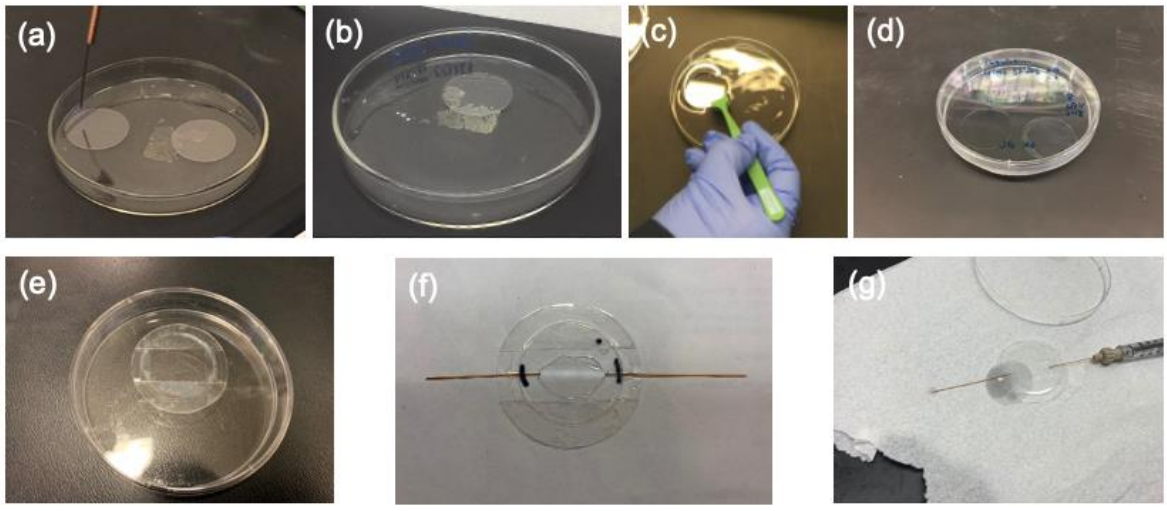

Figure 7.2: Actin flow chamber assembly and coating. (a) Plasma treatment and silanization. (b) Glass sandwich PEGylation coating. (c) Glass sandwich separation and washing. (d) PEGylated slides. (e) Flow chamber assembly (open setup). (f) Flow chamber assembly (sealed setup). (g) Flow chamber priming with syringe.

Flow chamber actin mounting and labeling:

The flow chamber channel prepared from the previous step was firstly incubated with 50 nM Neutravidin for 1 hour followed by twice DI water washing. Next, it was flowed with 50 nM Biotin-phalloidin for 1 hour followed by twice 1x imaging buffer (20 mM HEPES-KOH, 25 mM KCL, 1 mM $MgCl_2$, 1 mM EDTA, 1 mM APT, 1 mg/mL BSA and 0.4% Methylcellulose at pH 7.0) washing. Next, the polymerized actin (previously prepared following the procedure described in Chapter 6.3) was introduced to the channel and incubated under 4°C for 12 hours in order to bind actin to top surface. Then, functionalized gold nanorods (previously prepared following the procedure described in Chapter 6.3) were flowed and crosslinked with actin under 4°C for at least 1 hour. After crosslinking, the chamber with labeled actin can be used for following disassembly and imaging purpose. Detailed disassembly method and dynamics result are discussed in Chapter 8.1.

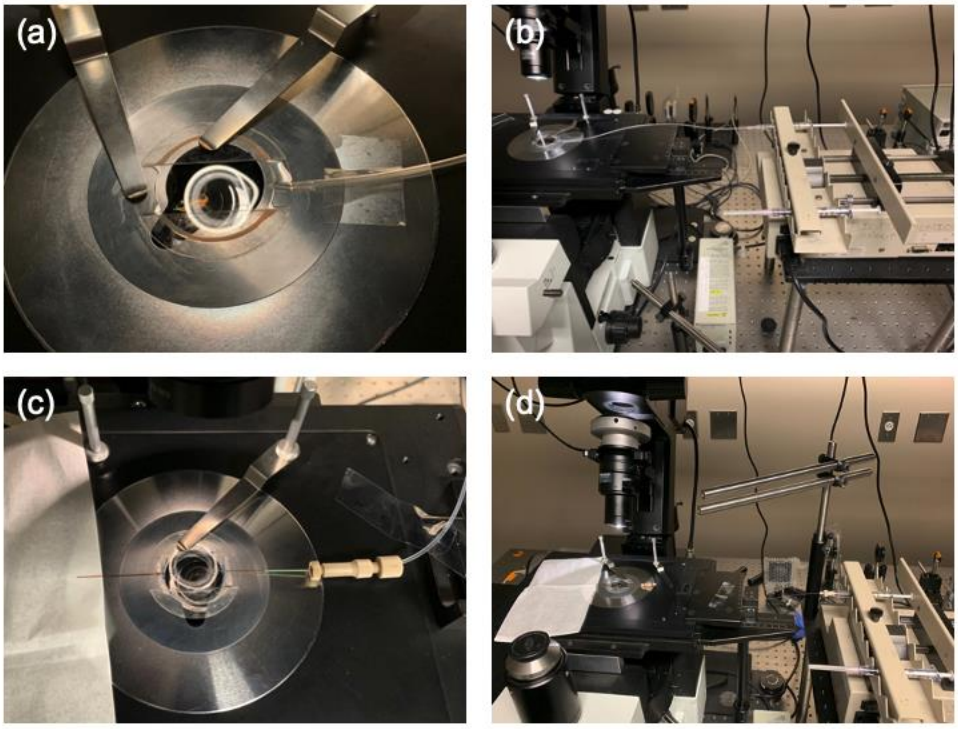

Figure 7.3: Actin flow chamber imaging system setup. (a)(b) Open setup chamber with inlet connected to syringe pump and outlet exposed to air. (c)(d) Sealed setup chamber with inlet connected to syringe pump and outlet connected to container.

Actin flow chamber imaging setup method:

For open flow chamber configuration, chamber contained labeled actin was firstly transferred to the microscope stage and secured by clips. A PE-90 (OD 1.27", ID 0.86") tubing was inserted into one side of the chamber, serving as the inlet (Fig. 7.3 (a)). The other side of the inlet tubing was connected to a syringe containing a certain buffer (ex. Cofilin in 1x imaging buffer for actin disassembly). A syringe pump (KD Scientific, 780220V) was used to continuously introduce buffer into the chamber at a low speed (1-3 μL/min) and activate the actin dynamics with binding protein (Fig. 7.3 (b)). For the sealed flow chamber configuration, the Luer-lock fitting adapter (Lab Smith, C360-300A) was placed between the syringe and capillary tubing for connection (Fig. 7.3 (c), (d)). Waste liquid was collected on the outlet side. The other parts of the setup were the same as the open flow chamber configuration.

7.3 Cell imaging chamber characterization and optimization

The environmental condition is vital to a closed on-stage cell imaging system. Among the factors discussed in Chapter 1, there are several that need to be discussed further during developing the imaging protocol.

Perfusion speed: Higher speed could ensure enough fresh media for the cell, while creating a higher shear force that could cause cell detachment from the slide. Also, it could cause turbulent flow that would cause the imaging quality to suffer by disturbing the cell debris. On the other hand, a low speed could also cause accumulation of chemicals due to not removing the old media in time.

Temperature: To create an ambient temperature (37°C) for cell growth, an evenly distributed temperature is necessary for the heating element selection and design. The exchanging

of the media as well as the distance between the incubator and chamber system could dramatically affect the dissipation of heating.

Tubing: A good selection of tubing material could help on heat insulation and keep heat dissipation to the minimum level. Due to the gas permeability of PE material, we kept input line short and protected by Tygon tubing.

Medium recycling: Recycling the media could be a wise option specially when the experiment is long. However, recycling the media too much is potentially bad for the cell growth due to the accumulation of harmful chemicals in waste medium.

Chamber thickness: The cell growth area was reflected on the chamber thickness, which is controlled by the gasket and its stacking numbers. A larger space is better for cell growth but could potentially slow down the heating and disturb the laminar flow.

In the protocol that I developed, these factors were characterized and optimized to achieve a stable environmental condition for long-term on-stage cell imaging. The detailed steps are discussed in below method sections.

Live cell labeling method:

Before setting up the chamber, SH-SY5Y cells were seeded and cultured on a cleaned 40 mm round glass slide with a PDMS well (25 mm*25 mm*5 mm) to reach 70% coverage. For better cell adhesion in the chamber, the glass slide was pre-coated with Fibronectin (0.5% in DPBS) for 45 minutes and then washed by DPBS once before seeding. Before adding the gold nanorods for cell labeling, the cell sample was firstly blocked by BSA (1.5% in warm cell culture media) for 20 minutes at 37°C. Then, the c4-antibody functionalized rod was mixed with the warm cell culture media and incubated over night with cells at 37°C for best surface actin labeling quality. The rest

of the cell seeding, culturing, and gold nanorod labeling procedures are same as described in Chapter 6.4.

Additionally, the live cell surface actin labeling quality under different labeling times (Appendix Fig. A.3) was also tested. Based on the observation, the optimized GNR cell incubation time was 12-hour (overnight). More detailed method and analysis are discussed in Appendix A.

Cell imaging chamber setup method:

After cell surface actin GNR labeling, a 30 mm round coverslip was firstly placed into the top plate of the warner chamber (Warner Instruments, RC-31 chamber). A thin layer of O-Ring grease was applied priorly to the outside edge of both plates to increase leak proofness of the system. A 375 μm thickness gasket (Warner Instruments, GS-30L/15) was then placed on the top plate tightly. The perfusion inlet and outlet ports of top plate were matched with the position of the gasket. Next, the 40mm round glass slide with cells was located on the platform base of the chamber. Additionally, 150 μL of warm cell culture media (DMEM, 10% FBS and 1% Penstrep) was added to the cells to keep surface from drying out. Finally, a top plate with a coverslip and gasket was assembled and matched into the platform base by aligning the cutouts of the top plate with the blocks of the base. Six screws were tightened for the whole chamber (Fig. 7.4 (c)).

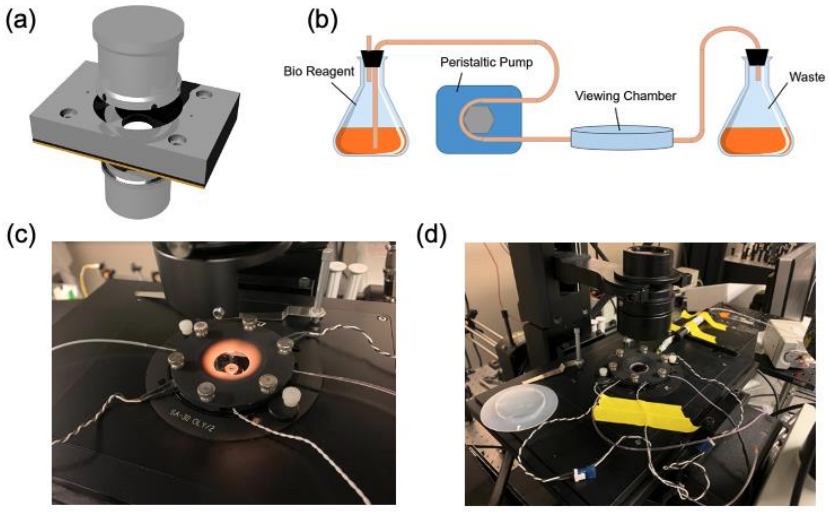

Figure 7.4: Cell imaging chamber setup. (a) Cell imaging chamber located on-stage between darkfield condenser and objective. (b) On-stage live cell culture achieved by perfusion system. (c) Close look of the on-stage cell imaging chamber. (d) Full setup.

To set up the imaging chamber on the microscope stage, a perfusion system was introduced (Fig. 7.4 (b)). Prior to the experiment, cell culture media was stored in a 50 mL centrifuge tube and warmed up in the standard incubator (37°C and 5% CO_2). One side of the input perfusion tubing (PE-160, OD 1.57", ID 1.14") was placed into the 50 mL centrifuge tube containing the media, while another side was connected to the chamber input port with a protection of Tygon tubing (ID 0.76 mm, OD 2.69 mm). The perfusion tubing was placed through a peristaltic pump (Instech laboratories, Model P720) for which the pumping speed was set to 0.1 mL/min to slowly perfuse media into chamber regularly. Priming (with max pumping speed as 0.5 mL/min) was done ahead of time to create bubble-free conditions in the perfusion tubing and the chamber. Perfusion outlet tubing was connected to transfer media into the waste container or to recycle the media back to its original tube. The cell imaging chamber was inserted to the stage through an adapter (Warner Instruments, SA-30 OLY/2) and located between condenser and objective lens (Fig. 7.4 (a), (c)).

For temperature control, the heater power and feedback lines were connected from the heater controller (Warner Instruments, Model TC-324C & TC-344C) to the warner chamber. The two blue-ended heater cables were connected to the two 2-prong cables, while a white feedback thermistor was inserted into the reflection hole of chamber. To directly monitor the temperature in the chamber more accurately, a thermistor could be directly inserted into the chamber. An in-line heater (Warner Instruments, SF-28) was also added before the chamber inlet as the media pre-heater. With the setting for the chamber heater (34.8°C), the in-line heater (37°C), the objective and condenser heater (Bioscience Tools, TC2-80-150) (37°C), the inside temperature of the chamber was maintained to 37°C ± 0.2°C (Fig. 7.6 (d)). Details of temperature control optimization is discussed in Chapter 7.4.

The full setup of the live cell imaging chamber system is shown in Fig. 7.4 (d).

7.4 Temperature control and flow rate optimization

Temperature is an important factor for long-term bio-imaging. Not only the bio specimens require a certain temperature to be biologically active, but temperature could also affect the dynamics of the sample, and further influence the imaging quality. Brownian motion, the random motion of particles suspended in a fluid resulting from their collision with the fast-moving atoms or molecules in the gas or liquid, is known to have a positive correlation with temperature[100].

By labeling actin filaments with GNRs to forming a network material, we found the opposite phenomenon from Brownian motion. To characterize the movement of actin, the maximum random moving distance of multiple randomly selected spots in an Actin-GNR network located was collected. The GNR labeled actin located in the flow chamber without disturbing the inlet flow. Three temperature points (25°C, 35°C, 45°C) were achieved and controlled by the objective lens heater and the same area of the Actin-GNR network was imaged under the darkfield

microscope (Fig. 7.5 (a)). The random motion of the GNR labeled actin network decreased while increasing the temperature (Fig. 7.5 (b)). In particular, under 25°C, an average of more than 600 nm movements were observed, while it was below 400 nm when heated up to 45°C. However, the difference between 35°C and 45°C was not large enough to increase the temperature further. Under higher temperature, the liquid sample will also suffer from evaporation. Therefore, for long-term imaging of actin, the samples in the flow chamber were heated and remained around 35°C, to achieve the optimal imaging quality.

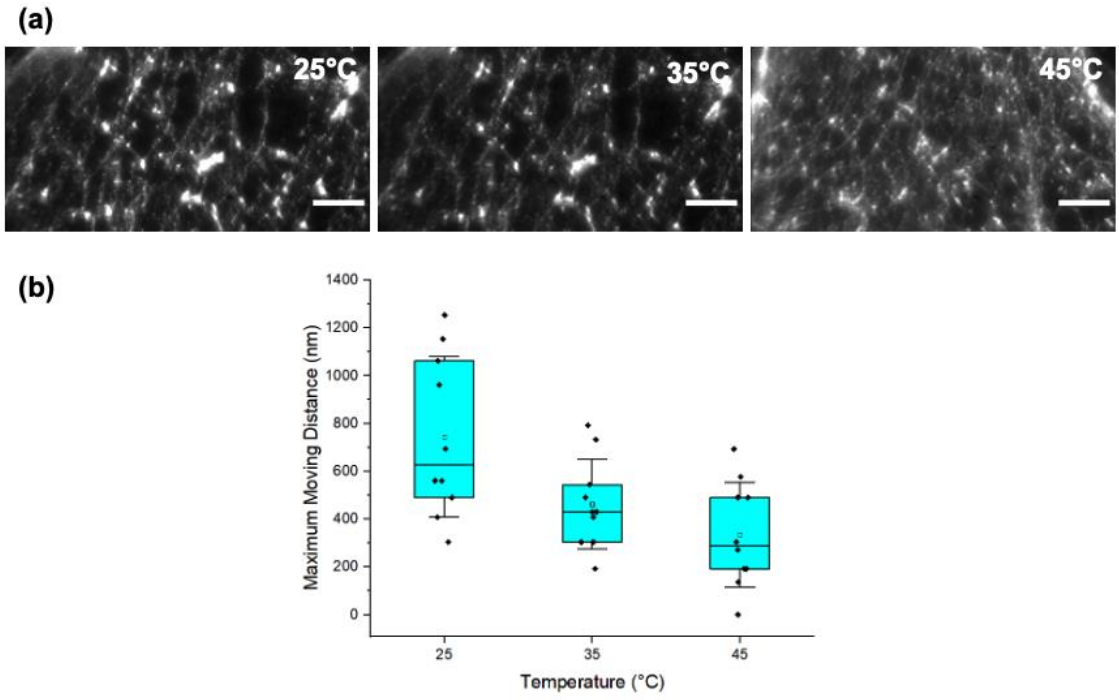

Figure 7.5: The random motion of GNR labeled actin network decreases as increasing the temperature. (a) The random-walk motion of a selected Actin-GNR network location was monitored under darkfield microscope, under 25°C, 35°C, 45°C respectively (controlled by objective lens heater). Images were taken under 40x objective continuously with 200 ms exposure time. (b) Temperature (°C) vs Maximum Moving Distance (nm). Scale bar: 5 μm.

For the long-term cell imaging in the cell imaging chamber, temperature control is even more crucial. Small temperature fluctuations will affect cell activities such as division and migration by influencing its fluidity and permeability[101]; too high or too low temperatures can cause serious

damage to the cell membrane[102]. In the worst case, exposure to an extreme temperature range can cause apoptosis to the cell. To create a good environment for on-stage live cell culture, the temperature in the chamber should be evenly distributed and controlled at 37°C with little fluctuation (< ±0.5°C). To achieve these conditions, the following aspects were considered: multiple heating elements in different locations, a feedback control system, good insulation between the heat transferring in the tubing and the direct temperature monitoring from the chamber.

The heating elements were selected and placed in different locations. The two regular chamber heating electrodes were located on the opposite sides of the chamber to be the main heater. The in-line heater of the tubing was to pre-heat the media to the designed temperature before introducing into the chamber. A feedback control system was used for both chamber heater and in-line heater, with the temperature monitored by the thermistor inserted to the chamber. Besides, a Tygon tubing was selected as the insulation for the PE tubing because of its low gas permeability. Moreover, both condenser heater and objective lens heater (Fig. 7.6 (a)) were used to decrease the temperature fluctuation. To verify the temperature control, I have monitored the temperature over a two-hour window while selecting one or multiple heating elements. With chamber heating as the only heating element, the media temperature in the chamber had a maximum fluctuation of 0.6°C with an average of 37.04°C (Fig. 7.6 (b)). With the addition of the condenser heater (Fig. 7.6 (c)) and objective heater (Fig. 7.6 (d)), the temperature fluctuation could be kept under 0.5°C with an average of 37.02°C.

CO_2 level is another important factor in long-term cell imaging. CO_2 serves a non-metabolic role in cell cultures, as it dissolves into the culture medium. A fraction of it undergoes a reaction with water to create carbonic acid, which then interacts with the dissolved bicarbonate ions in the medium. This interaction regulates a consistent physiological pH via the bicarbonate buffering

system. 5% CO_2 is a standard requirement for cell culture and tissue culture to keep the pH value in the proper range which is 7.2 to 7.4[103]. In our setup, the CO_2 level was controlled using the incubator which also had the function of warming up the media. With the gas insulation for the tubing and the gas proofing of the warner chamber system, a constant CO_2 level was achieved in our system (Fig. 7.6).

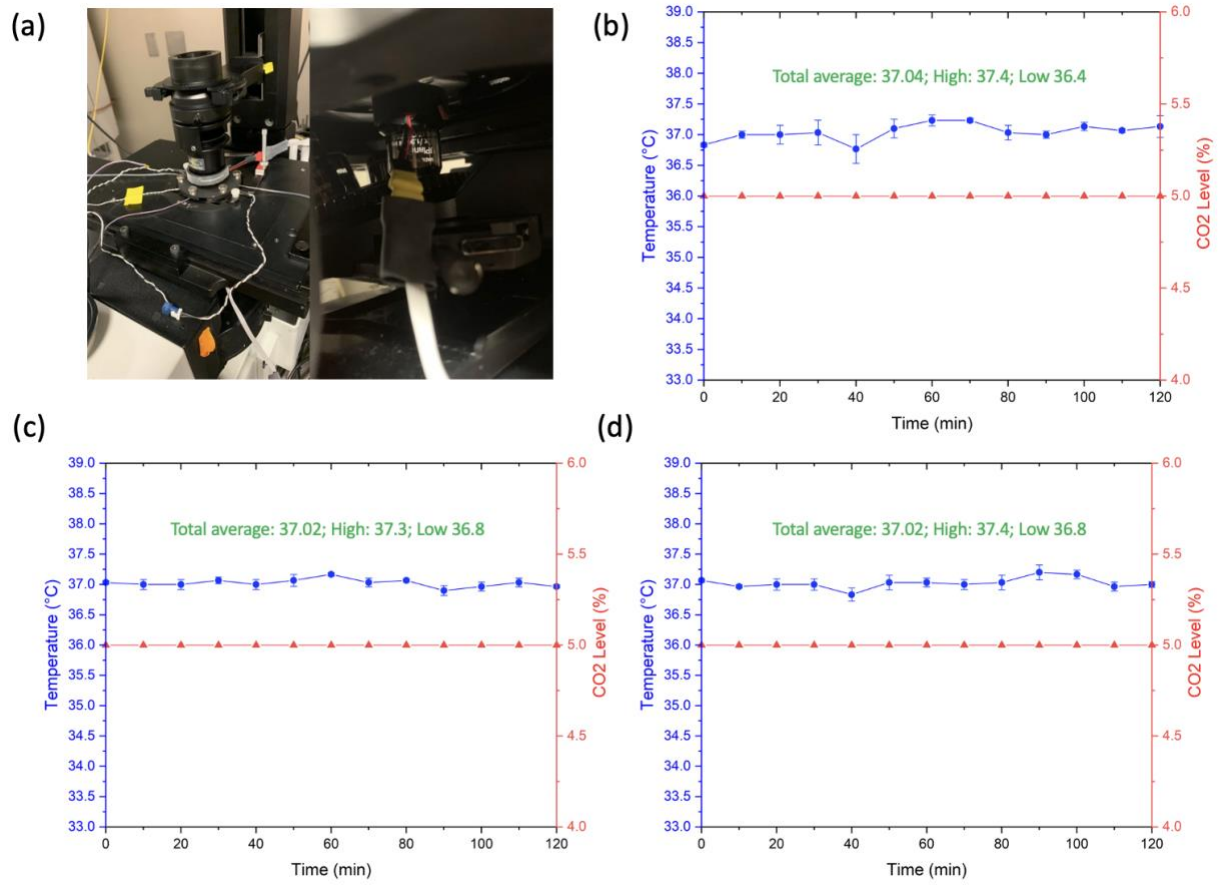

Figure 7.6: Heating and CO_2 control optimization. (a) Left: Chamber heater and condenser heater; Right: Objective heater. Chamber temperature (°C) and Chamber CO_2 level (%) vs Time (min) with (b) only chamber heater; (c) chamber and condenser heater; (d) chamber, condenser, and objective heater.

Laminar flow characterizes the smooth, orderly movement of a fluid (gas or liquid) as it travels along predictable paths, differing from turbulent flow where irregular fluctuations and mixing occur (Fig. 7.7 (a)). Laminar flow typically occurs in confined spaces, slow-moving fluids,

and those with higher viscosity, such as within microfluidic environments. Qualitatively, one can distinguish the type of flow using fluid motion and speed. On the one hand, the motion of high viscosity fluids at low speeds is generally laminar. On the other hand, a high degree of irregular fluid motion at high speeds is defined as turbulent. Quantitively, Reynolds number plays a crucial role in determining whether the flow will be laminar or turbulent. A lower Reynolds number indicates laminar flow, while a higher value leads to turbulent flow in fully developed flow conditions.

Reynolds number is calculated using:

$$Re = \frac{\rho u L}{\mu} \tag{7.1}$$

Where ρ is the density of the fluid; u is the velocity of the fluid; L is the typical length scale, and μ is the dynamic viscosity of the fluid. The numerical values used in the calculation for our cell imaging chamber are: ρ = 1 g/mL, L = 0.2 mm, μ = 8.94×10^{-4} Pa·s. The relationship of Reynolds number and flow rate (μL/min) was characterized in Fig. 7.7 (b). To maintain a pretty good laminar flow, the general rule of thumb is Re < 2000[104]. Therefore, the flow rate from the perfusion pump should set to below 10 μL/min. Practically, I have also visualized the laminar flow in the actin flow chamber by using different dyes. The concentration gradient was achieved by adding a triangle divider on the inlet to separate the top and bottom flows (Fig. 7.7 (c)). The flow rate was set to 5 μL/min using a syringe pump. The separation of the two flows demonstrated the laminar flow for the chamber, as well as presenting an opportunity for multi protein activity observations in a single experimental run in the future. The gradient of the concentration also verified my observation of actin network disassembly by cofilin, which had a higher occurrence rate near the inlet compared with the outlet side.

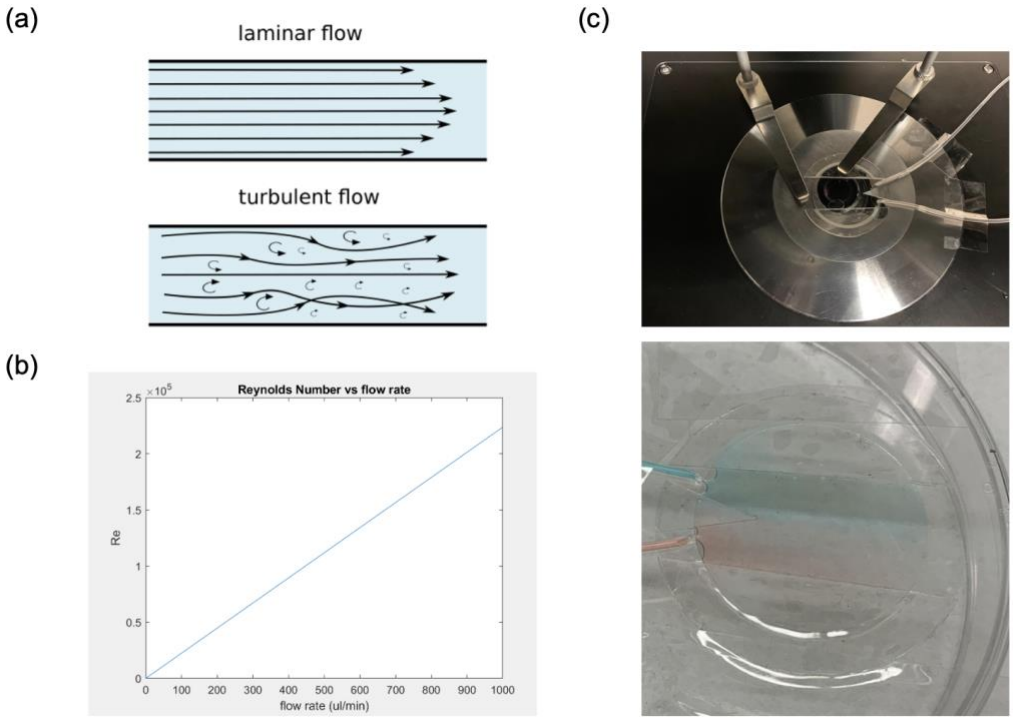

Figure 7.7: Laminar flow, turbulent flow, and Reynolds number. (a) Laminar flow vs turbulent flow. (b) Reynolds Number (Re) vs Flow Rate (μl/min). (c) Top: Laminar flow demonstration on-stage setup; Bottom: Laminar flow and concentration gradient were demonstrated by blue (top) and red (bottom) dyes in the actin flow chamber using a 5 μL/min flow rate.

In conclusion, this chapter delved into the design and optimization of the imaging system for long-term protein and cell dynamics imaging. Firstly, an actin flow chamber setup was proposed, which utilized gold nanorods (GNRs) as plasmonic labels for actin filaments, employing silanization and PEGylation as mounting mechanisms. Essential steps for setting up the actin flow chamber before commencing long-term imaging experiments, such as chamber assembly, coating, and pumping system setup, were also discussed. Subsequently, a protocol was developed following the optimization of environmental factors to establish a stable closed-chamber system for long-term on-stage cell imaging. Specifically, temperature stability was characterized through the

random motion of actin filaments. Additionally, laminar flow within the chamber was achieved and demonstrated via concentration gradients of the fluid.

Chapter 8 Actin Dynamics Imaging

8.1 Actin filament dynamic imaging

Previous work[60] showed the crossover length of an actin filament shortens from 2.2 subunits to 2.1 subunits under the presence of cofilin. That is due to cofilin changing the twisting angle of the actin filament, leading to the rotation of the actin. Through our new approach, we can characterize the rotation induced by cofilin through the polarization property of gold nanorod. By applying a linear polarizer and tracking the intensity of the gold nanorods for each polarization state, we could extract the orientation of each particle binding to the actin filament, and then, characterize the actin rotation behavior.

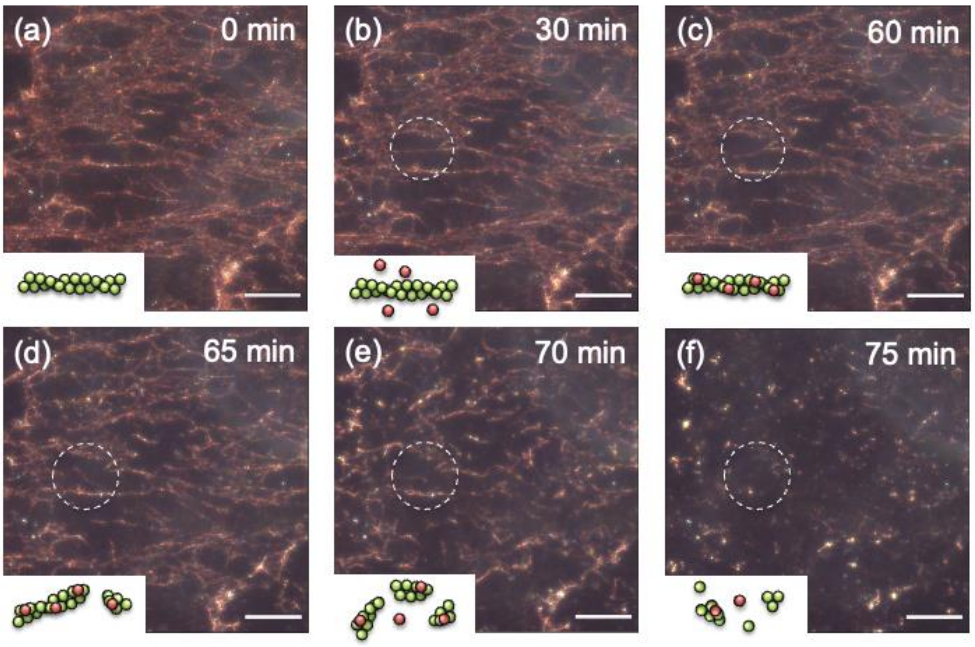

Figure 8.1: Continuous, long-term imaging enables quantitative analysis of actin dynamics by cofilin. Cofilin was introduced at 30 min. Diagram: Green dot (actin); Red dot (cofilin). Scale bar: 10 μm.

Fig. 8.1 shows the darkfield images of cofilin severing and disassembling actin network visualized using gold nanorods. The sample images without presence of cofilin are shown in the first two images (0-30 min), and the sample images with presence of cofilin are shown in the images taken between 30-75 minutes. We first demonstrated that the actin filaments were successfully labeled by GNRs with high-density and high efficiency (Fig. 8.1 (a)). The Actin-GNR network was formed and mounted on the top surface of the chamber. Without the presence of cofilin (0-30 min), the gold nanorods can outline the shape of actin filament and may be distinguished from the background. The shape of the actin network remained unchanged in the first 30 minutes (Fig. 8.1 (b)). With the presence of cofilin (30-75 min), the actin filament length reduced over time, and actin network was severed by cofilin in multiple places (65-70 min) (Fig. 8.1 (d), (e)). After 75 minutes, most of the shortened actin filaments in the view disappeared due to the flow (Fig. 8.1 (f)). The enlarged images (Fig. 8.2) show a single actin filament being severed by cofilin between 60-65 minutes. The left end of this filament was first cut at 60 minutes (Fig. 8.2 (b)), while the right end was cut at 65 minutes (Fig. 8.2 (c)), and fully released the actin filament. Besides, the severing happened in the presence of cofilin also proves the actin filaments were still biologically functional after labeled with the gold nanorods. The continuous imaging enables the possibility of capturing long-term processes.

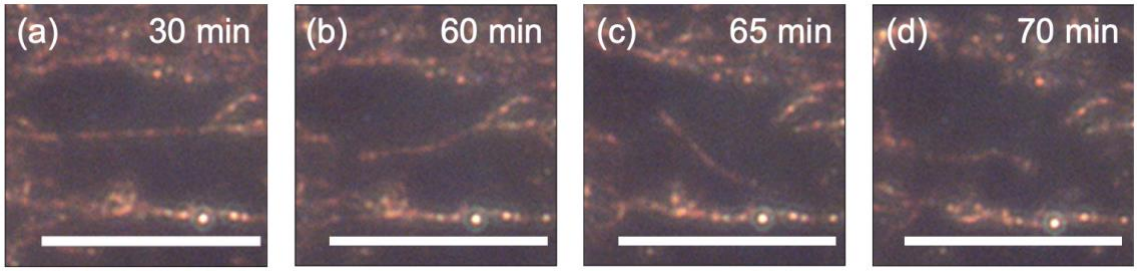

Figure 8.2: Actin dynamics between 30 min and 70 min of the enlarged circled area from Figure 8.1. Scale bar: 10 μm.

The optical stability of plasmonic labeling method was also demonstrated during the actin filament dynamics imaging (Fig. 8.3). Actin filament was labeled with both plasmonic marker (GNR) and fluorophore (Alexa Flour 488), and continuously observed for 50 minutes during actin cofilin dynamic. The intensity of fluorescent labeled actin network (control) rapidly decreased to 0.3 within 15 minutes due to photobleaching. By contrast, the GNR labeled actin network (darkfield) was not suffered with photobleaching and maintained at high intensity over the time course. The slight decrease of intensity in darkfield was due to morphology changing of the actin network during slow dynamics. The plasmonic labeling method opens the window for continuously capturing slow dynamics such as actin disassembly over long period of time.

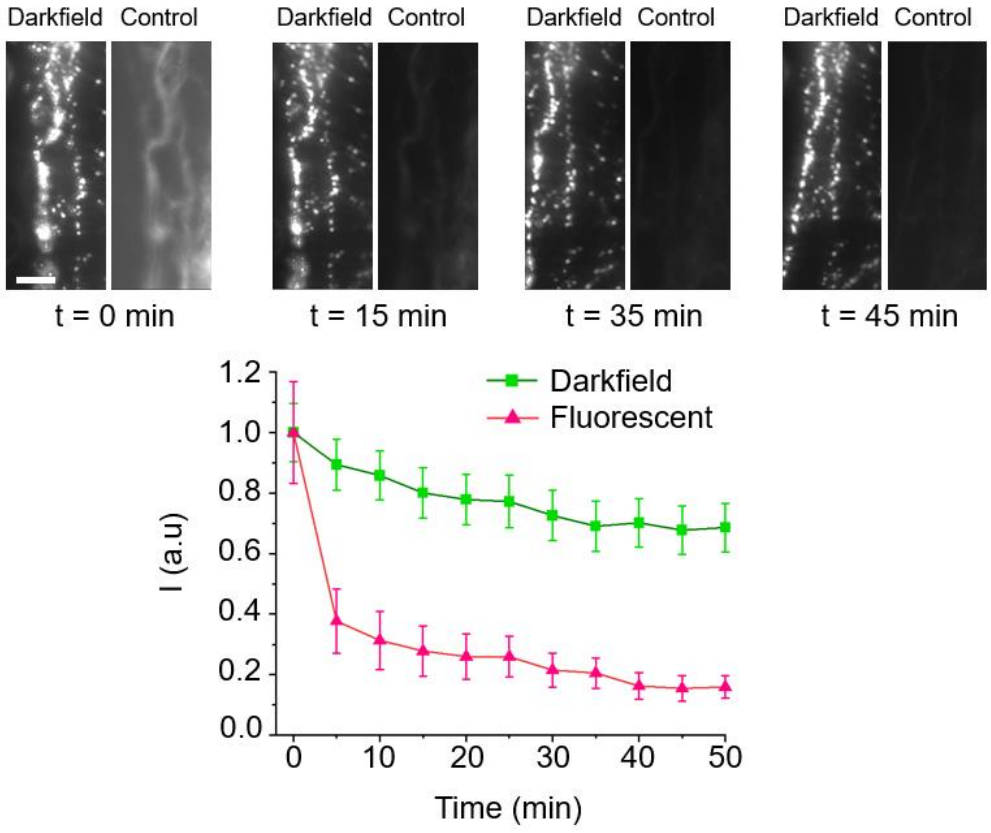

Figure 8.3: Plasmonic labeled network are optically stable during long-term slow dynamic imaging free from photobleaching. Time course fluorescent actin images (control) and GNR labeled actin images (darkfield) taken over 50 min. In each time course image, intensities were averaged together and plotted on below graph. Time course graph comparing scattering intensity (green) vs fluorescence intensity of control (pink). Scale bar: 10 μm.

Actin cofilin disassembly and imaging method:

After the flow chamber assembly, coating, F-actin mounting and labeling (Chapter 7.2), the flow chamber with the gold nanorod labeled actin was transferred to the microscope stage for imaging purpose (Fig. 7.3). Cofilin (2.6 μM in 1x KMEI buffer) was introduced to the channel through PE-90 tubing. A constant flow rate (2 μL/min) was controlled using a syringe pump. The darkfield images of Fig. 8.1 and 8.2 were taken with a Retiga 3000 color CCD (exposure time 300 ms), and a 40x objective (Olympus, UPLFLN40X N1478600).

8.2 Actin dynamics quantification and analysis

There are two aspects that I used to quantify actin cofilin disassembly dynamics, orientation, and length. The orientation distribution of the actin network is an indicator for slow dynamics such as cofilin disassembly or actin bundle formation. Fig. 8.4 shows the orientation change of an Actin-GNR network with or without the presence of cofilin. Noted that the initial states of orientation distribution were different between the two samples. For the control sample, filaments were more evenly distributed over 360°. In the sample with cofilin, fewer filaments were distributed horizontally (0° and 180°) than vertically (90° and 270°), leading to a narrow orientation distribution. The difference was because of the random selection of the field of view in each sample. Without the introduction of cofilin (control), the Actin-GNR network remained mostly in its original orientation over 80 minutes (Fig. 8.4 (a)). Although the filaments randomly swung through the flow, there was limited orientation changes. In presence of cofilin, actin filaments were severed, leading to significant orientation changes of the whole the network (Fig. 8.4 (b)). The changing of orientation started 40 minutes after the cofilin introduction, which

matched the visual observation in Fig. 8.1. The majority of the actin filaments were disassembled by cofilin within 80 minutes.

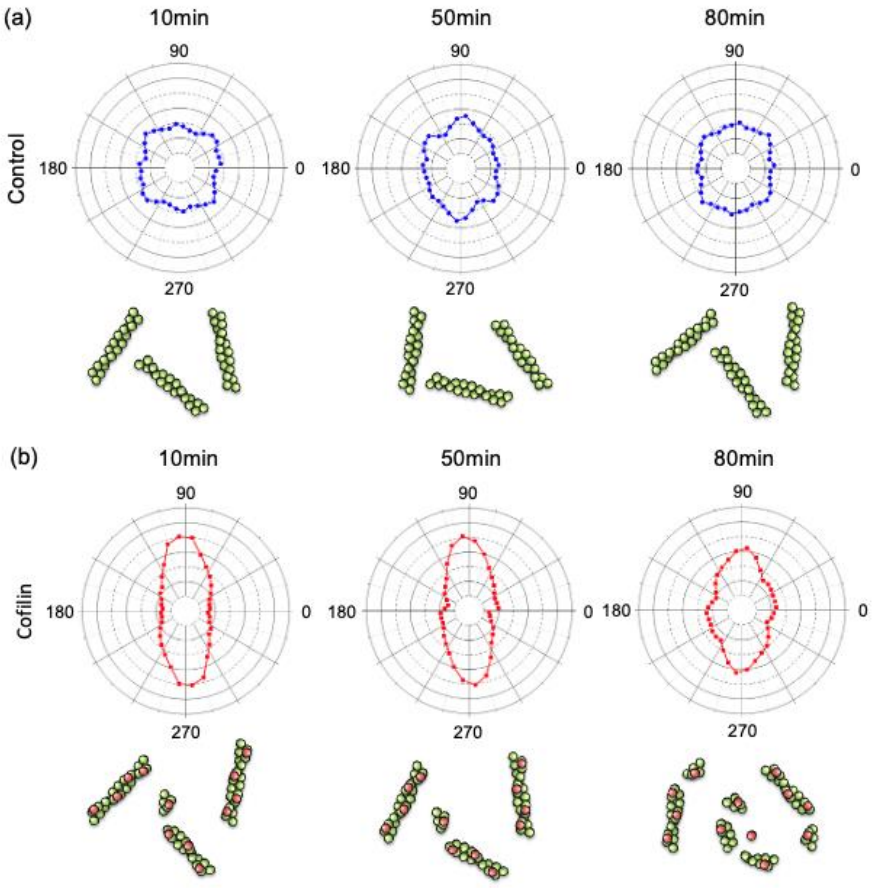

Figure 8.4: Actin filaments orientation distribution over 80 min with or without the presence of cofilin. (a) No significant orientation difference in the control sample. (b) Cofilin was introduced at 10 min, leading to significant orientation change of the whole network within 80 min due to severing.

Length of the actin filament is another useful indicator to show slow dynamics. For example, in bundle network formation, multiple single actin filaments tend to bundle together to form a thicker bundle that tangles together, leading to length change among the whole network. Our case is the opposite to the bundling, where cofilin severing would cause shrinking and disassembly of the actin network. The length of each filament would be shortened significantly, with an increase of total filament quantity due to filaments severing. However, the total quantity might be difficult to represent slow dynamics under the current experimental setup. Due to the constantly flow,

instead of hanging around their original location, most of the severed actin filaments are washed away by the flow. That would cause the decrease of total actin filament number which was opposite to the prediction. One possible solution to overcome this problem is to change the method of cofilin introduction from flow to gravity dropping. In this case, the whole view of actin network would be under stable condition without disturbed by the extra flow. The challenge of this method is to add cofilin without influencing the actin in the field of view. This can be done using a lower magnification of objective lens which would sacrifice the spatial resolution.

As shown in Fig. 8.5 actin filament length was measured over time with the presence of cofilin. Three cofilin concentrations were tested here: no cofilin (control, orange), 2.38 μM (red) and 4.76 μM (blue). In Fig. 8.5 (a), each data point indicates a single actin filament with a certain length. While the length of actin filaments in the control sample (orange) remained unchanged, which indicates no dynamics occurred, in the two samples with cofilin, the length of filaments all reduced over time. Specially, in the sample with a higher cofilin concentration (blue), complete disassembly happened after 40 min, bringing most of filament lengths to zero. Fig. 8.5 (b) shows the average filament length of each sample changing over the slow dynamics. It was more obvious that in absence of cofilin, the average actin filament length remained constant. And with presence of cofilin, average actin filament length reduced over time by 5.17 μm (in 2.38 μM cofilin) and 21.79 μm (in 4.76 μM cofilin). We found an almost 4 times length reduction when doubling the cofilin concentration. During the rapid disassembly period (35-45 min) for the high cofilin concentration, the actin disassembly rate increased from 0.06 μm/min to 2.07 μm/min (in 4.76 μM cofilin).

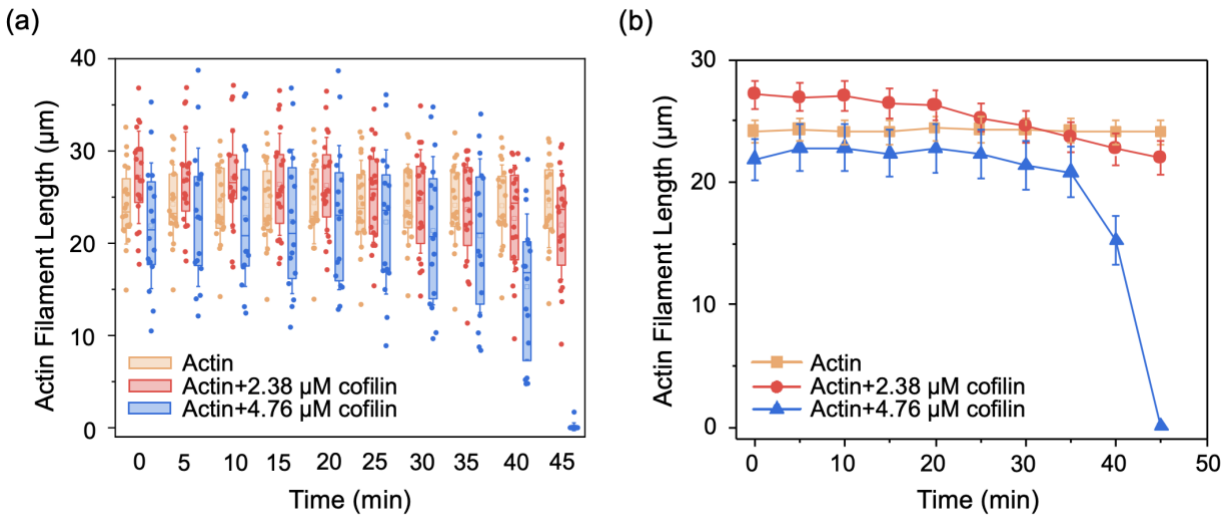

Figure 8.5: Quantitative analysis of actin disassembly by cofilin. (a) Actin filament length distribution (μm) vs time (min) under different cofilin concentrations (0, 2.38 μM and 4.76 μM). (b) Actin average length (μm) vs time (min) under different cofilin concentrations (0, 2.38 μM and 4.76 μM).

Next, I applied the plasmonic labeling method to live cell imaging, targeting the extracellular β-actin dynamics during cellular activities such as cell migration and division, and utilizing the live cell imaging system discussed in Chapter 7. First of all, 30 minutes of continuous cell migration imaging was achieved in the cell imaging chamber for both GNR labeled cell (Appendix Fig. B.1 (a)) and unlabeled cell (Appendix Fig. B.1 (b)). Obvious cell migration was observed in both samples with similar migration speeds over 30 minutes. That not only demonstrated the feasibility of our live cell imaging system in terms of long-term imaging, but also indicated the plasmonic label didn't have any negative impact on the functionalities of the cells. In addition, continuous imaging of single-cell division was also demonstrated through our live-cell imaging system (Appendix Fig. B.2). Clear dynamics of cell membrane surface area was also observed during one cycle of cell division through cell area quantification (Appendix Fig. B.2 (a)).

The orientation distribution of extracellular β-actin is also an indicator of cell cycle phases. As shown in Fig. 8.6, actin filament orientations (measured by GNR) under four different phases of the cell cycle were quantified using a plasmonic nanoscope.

In the initial stages of cell division, specifically during the prophase and metaphase, the gold nanorods (GNR) exhibited a uniform distribution across all orientations, maintaining consistency between these two phases. This uniform distribution indicated the random arrangement of surface β-actin. Subsequently, in the cell division's growth phase (G phase), as microtubules continued to exert force to separate the two cells, the orientation of the GNR notably aligned perpendicular to the direction of cell separation. This directional alignment corresponded to a more orthogonal distribution of surface actin.

Finally, during the telophase, which marks the last phase of mitosis, a cleavage furrow emerged to facilitate complete separation between the two cells. At this stage, the orientation of the GNR returned to a more standard or normal distribution pattern.

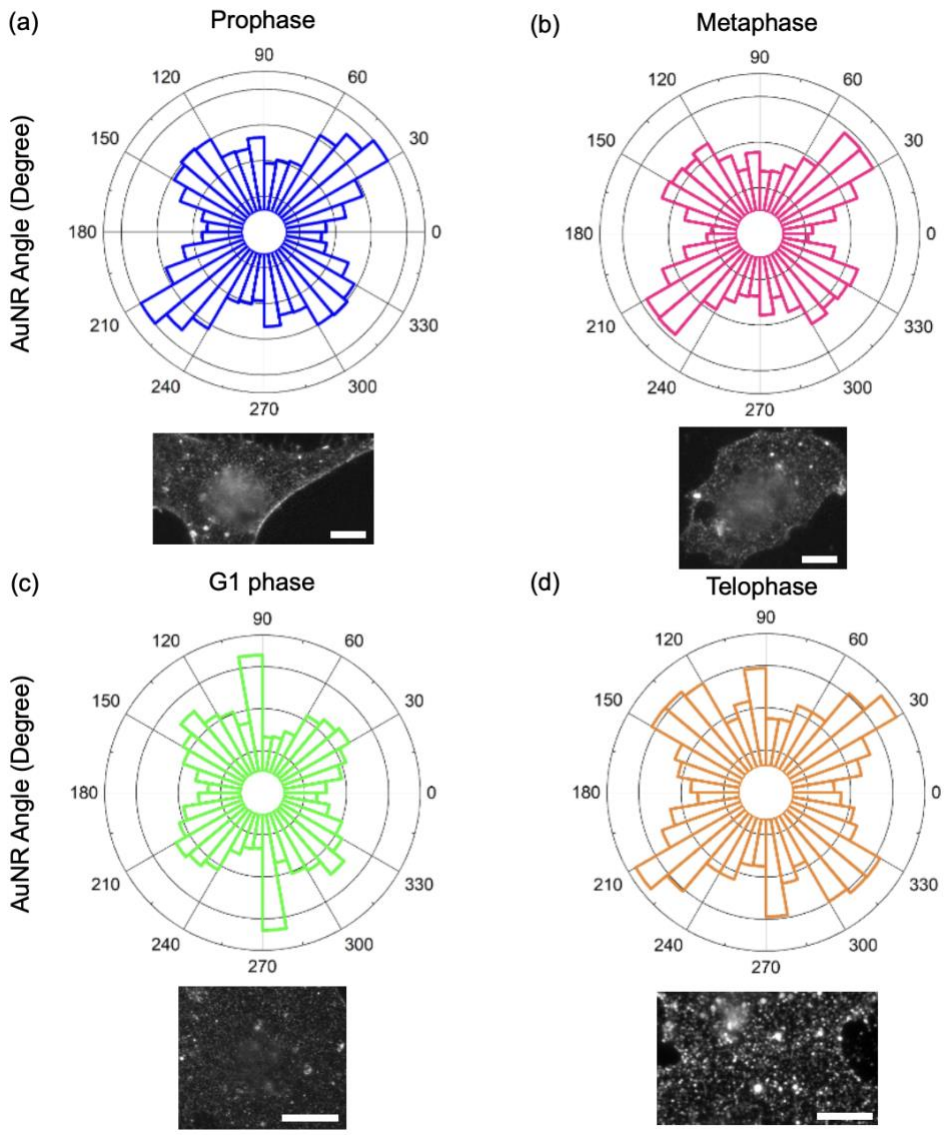

Figure 8.6: Extracellular β-actin filament orientation distribution measured by GNR and nanoscope images under four different phases of the cell cycle: (a) Prophase; (b) Metaphase; (c) G1 phase; (d) Telophase. Scale bar: 10 μm.

In conclusion, we demonstrated continuous, long-term imaging of actin disassembly dynamics by cofilin, followed by quantification analysis using our plasmonic nanoscope imaging system. The optical stability of the plasmonic probe was also showcased during the imaging of actin dynamics, providing a comparison with fluorophore-labeled actin filaments. Specifically, the orientation and length of actin filaments were characterized using the plasmonic nanoscope during

the gradual dynamics of cofilin disassembly. Furthermore, the plasmonic labeling method was applied to live cell imaging, targeting extracellular β-actin dynamics during cellular activities. We demonstrated that the orientation distribution of extracellular β-actin strongly correlated with different cell cycle phases. Additionally, continuous cell migration imaging and single-cell division imaging were achieved in the live-cell chamber system, which shows the capability of this non-bleaching, continuous imaging method on capturing different long-term processes.

Quantitative analysis and simulation method:

The quantitative data relating to the actin filaments such as length, orientation and filament number were obtained from the high-resolution images (discussed in Chapter 6.5) through Fiji (Ridge Detection), then analyzed by code performed in MATLAB (MathWorks) and plotted. The images of Fig. 8.3 were taken every 10 minutes for 80 minutes and the contrast was adjusted to 0-55 for all images. The ridge detection settings were: Line width = 10; High contrast = 255; Low contrast = 30; Sigma = 3.39; Lower threshold = 0.1; Upper threshold = 0.3; Minimum line length = 0; Maximum line length = 10.

The cell membrane surface area in Appendix Fig. B.2 was measured by pixel through Fiji, then analyzed by code performed in MATLAB (MathWorks) and plotted.

Chapter 9 Conclusion and Future Work

9.1 Overcoming challenges of long-term imaging

In summary, a novel nanoscale imaging method utilizing plasmonic nanoscope has been successfully developed to address the challenges encountered in long-term bio-imaging. This innovative approach ensures long-term non-bleaching and high photostability during imaging processes. Demonstrations included continuous visualization of actin and cellular dynamics spanning hours to days.

This method commenced with the development and optimization of a non-bleaching plasmonic labeling technique. Overcoming the limitations of short imaging windows due to fluorophore photobleaching was achieved through the utilization of gold nanorods as molecular markers. An application demonstration involved the visualization and quantitative analysis of actin dynamics during the disassembly process by actin binding protein (cofilin). Furthermore, the integration of nanoscale plasmonic nanoscopy enabled the analysis of the angular distribution of the gold nanorods within the actin network during gradual disassembly.

Addressing the challenge of phototoxicity in long-term single-cell imaging, the plasmonic labeling method was effectively applied to live cell labeling, specifically targeting extracellular β-actin on cell surface. To ensure successful long-term imaging, multiple aspects were considered and optimized within the long-term imaging platform. This includes design modifications of the flow chamber, temperature regulation, and optimization of flow rates. Protocols involving chamber assembly, coating, and the setup of live-cell perfusion systems were optimized to achieve optimal optical stability and resolution for long-term live-cell imaging. Ultimately, extended

observation of cell surface actin during fundamental cellular activities such as cell division and migration was achieved by establishing long-term imaging system and utilizing plasmonic nanoscope.

9.2 Future work

One of the limitations of our current plasmonic imaging system is the size of the nanoprobe, which impacts the scattering efficiency. There's a tradeoff between resolution and labeling densities of the small gold nanorods that must be carefully considered and tested. Another limitation is the sample depth, which currently restricts exploration in 3-D imaging along the z-axis. Moving forward, our method is poised for advancement and diverse applications on multiple fronts.

For immediate developments, we anticipate further exploration into surface β-actin remodeling on live cells during various cell activities, such as organelle movement. Utilizing the super-resolution capabilities of PINE, we aim to enhance the quantification of surface actin movement, enabling the development of a comprehensive visual model for extracellular β-actin dynamics. The application of our plasmonic imaging and quantification method can be extended to explore other protein-nanoparticle hybrid materials, such as lipid rafts[105]. This extension will facilitate comprehensive studies of such materials, providing invaluable insights into their structural and functional characteristics. The challenges associated with such applications include achieving specific labeling for selected organelles or proteins, as well as the need for a more advanced imaging system with higher capturing speeds to accommodate potentially faster movements of the target organelles or proteins[106].

For long-term developments, our goal is to enhance the speed of the current super-resolution imaging method to achieve real-time nanoscale imaging. Increased imaging speed is

crucial for capturing transient protein/cell dynamics and minimizing the spatial movement of gold nanoparticles in the fluid, thereby further enhancing resolution for live sample imaging. Achieving this needs optimization on both hardware and software fronts. Hardware optimization involves the development of faster liquid crystal-based PI with microsecond response times, a high-speed CCD for synchronization with PI, downsizing of gold nanorod dimensions for higher density labeling and reduced mobility. The challenges of such an upgrade include overcoming the sub-microspatial movement of plasmonic markers, which can be caused by Brownian motion or random walk. A fast and reliable autofocus system is needed to address this issue. Additionally, with the current seed-mediated growth method used for gold nanorod synthesis, there exists a balance between nanorod dimensions, yield, and synthesis quality that needs to be carefully managed.

On the software front, optimizing post-image processing is crucial for live nanoscale imaging. While our current deconvolution method delivers sub-10 nm resolution, it suffers from extended processing times. The integration of machine learning technologies such as Convolutional Neural Networks (CNN)[107] or Generative Adversarial Networks (GAN)[108] commonly utilized in computer vision and super-resolution image processing, is expected to significantly reduce post-image processing times. The challenges of applying machine learning (ML) to achieve real-time imaging are multifaceted. Firstly, a large image dataset comprising diffraction-limited images and corresponding ground truth data is necessary for training and optimizing the neural network effectively. Moreover, fast data transfer capabilities are essential for seamless real-time visualization of imaging results. These challenges highlight the importance of robust data infrastructure and algorithmic optimization in ML-driven imaging applications.

Furthermore, with the current method, we were able to label only one target protein. There is potential in exploring the simultaneous labeling of multiple targets with different plasmonic

probes. To achieve this, a mixture of gold nanorods with more diverse aspect ratios is necessary in terms of creating a substantial separation of their respective resonance frequencies. This avenue warrants further investigation to enhance the capabilities and versatility of the imaging system.

APPENDICES

Appendix A: Gold Nanorod Actin Conjugation Recipe Optimization

For the method used to test EDC and MC concentration in Appendix Figure A.1, different concentrations of EDC were adjusted during GNR functionalization step, and different concentrations of MC were added during crosslinking step. The GNR concentration was set to 0.2 nM and 2-mercaptoethanol quenching volume was set to 1 μL for all test samples. All other gold nanorod actin conjugation procedures followed the recipe described in Chapter 6.3.

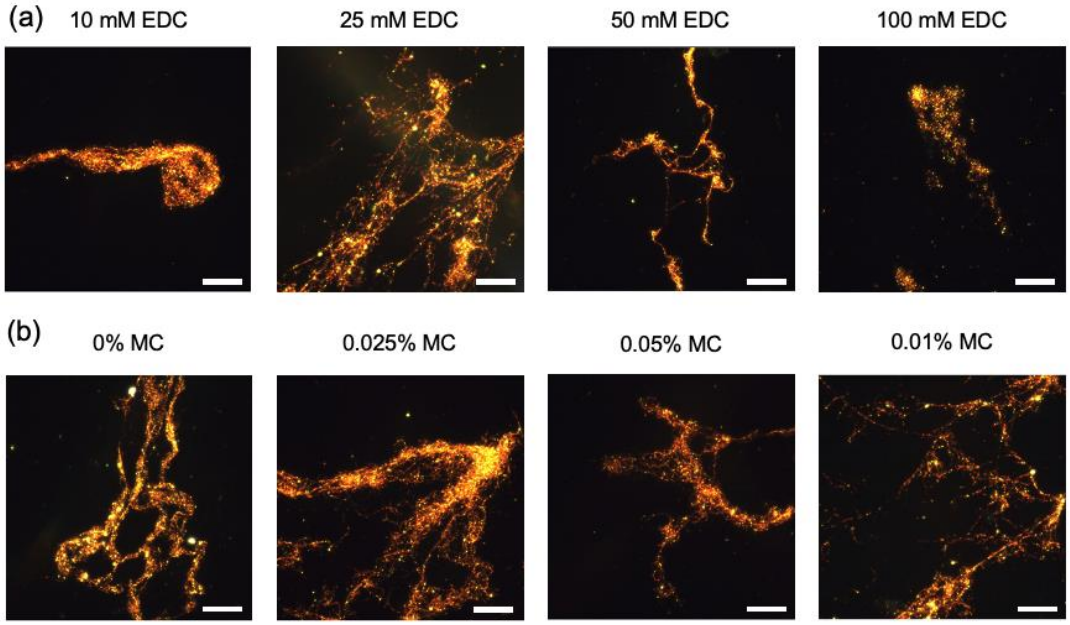

Appendix Figure A.1: Darkfield images of Actin-GNR network under different concentrations of EDC and MC (methylcellulose). (a) Actin-GNR images with presence of 10 mM, 25 mM, 50 mM, and 100 mM EDC. (b) Actin-GNR images with presence of 0%, 0.025%, 0.05% and 0.01% MC. Scale bar: 10 μm.

For the analysis method used to quantify labeling quality in Appendix Figure A.2, the crosslinker distances were obtained from the darkfield images through Fiji (Ridge Detection), then analyzed by code performed in MATLAB (MathWorks) and plotted.

As shown in Appendix Figure A.2 (a), the network appeared to have shorter average crosslinker distance as EDC concentration increased. Once EDC concentration drops below 20 mM, the network tended to be more aggregated, leading to a smaller crosslinker distance. There was an obvious trend that the crosslinker distance decreased with increasing EDC concentration whereas we might expect a negative correlation. The reason of slightly higher crosslinker distance under 400 mM EDC than 200 mM EDC was because the aggregated network was distributed more sparsely in the specific sample, which also increased the error bar of that data point (200 mM). Appendix Figure A.2 (b) shows now the average crosslinker distance slowly increased with increasing MC concentration. The reason for this could be slight variations of techniques when making the network samples.

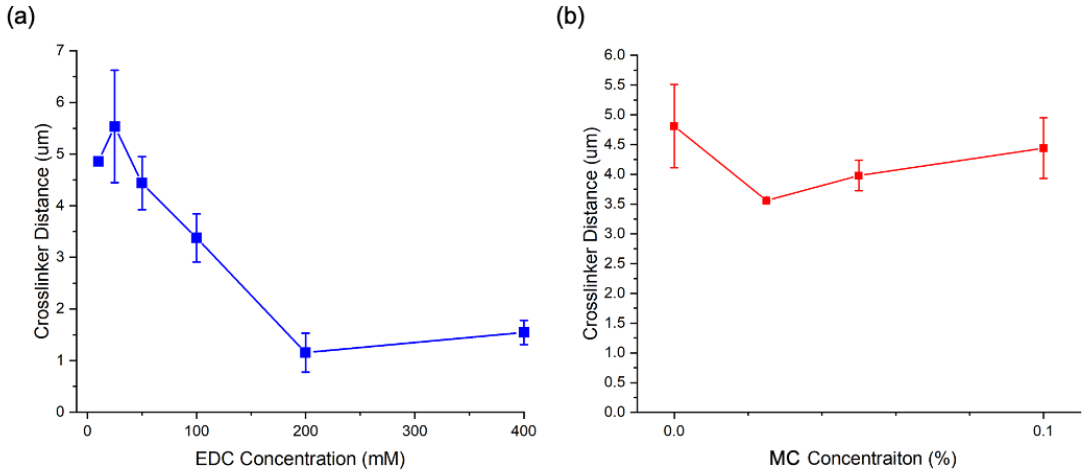

Appendix Figure A.2: The crosslinker distance (μm) of Actin-GNR network vs (a) EDC concentration (mM) and (b) MC (methylcellulose) concentration (%).

The recipe of live cell labeling was also optimized by testing the SY5Y and GNR incubation time. As shown in the Appendix Figure A.3, the 12-hour/24-hour didn't have much difference with respect to labeling quality, while the 3-hour sample was slightly less labeled. The control group with non-functionalized GNR shows the high selectivity of this labeling technology. For the method used in this experiment: 50 μL of OD 50 antibody functionalized GNR was mixed with 450 μL cell culture media for each sample. All other cell surface labeling procedures followed the protocol described in Chapter 6.4 and Chapter 7.3. The image was taken using a 60x objective with an exposure time of 200 ms (darkfield) or 300 ms (polarized darkfield). The microscopy setup is described in Chapter 6.5.

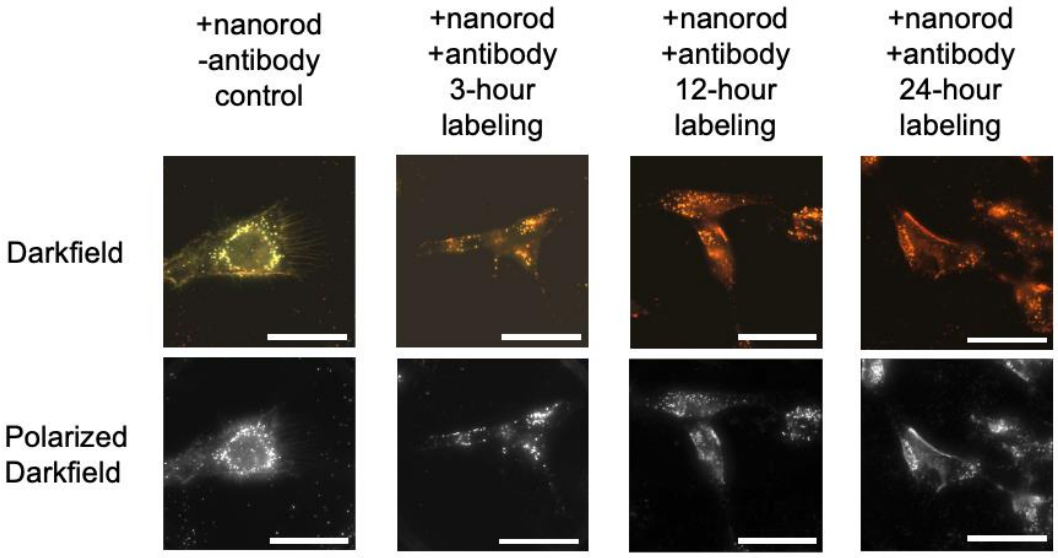

Appendix Figure A.3: Darkfield and polarized darkfield images of GNR labeled live cell under different labeling times: control, 3-hour, 12-hour, and 24-hour. Scale bar: 50 μm.

Appendix B: Long-term Live-cell Imaging of Cell Migration and Division

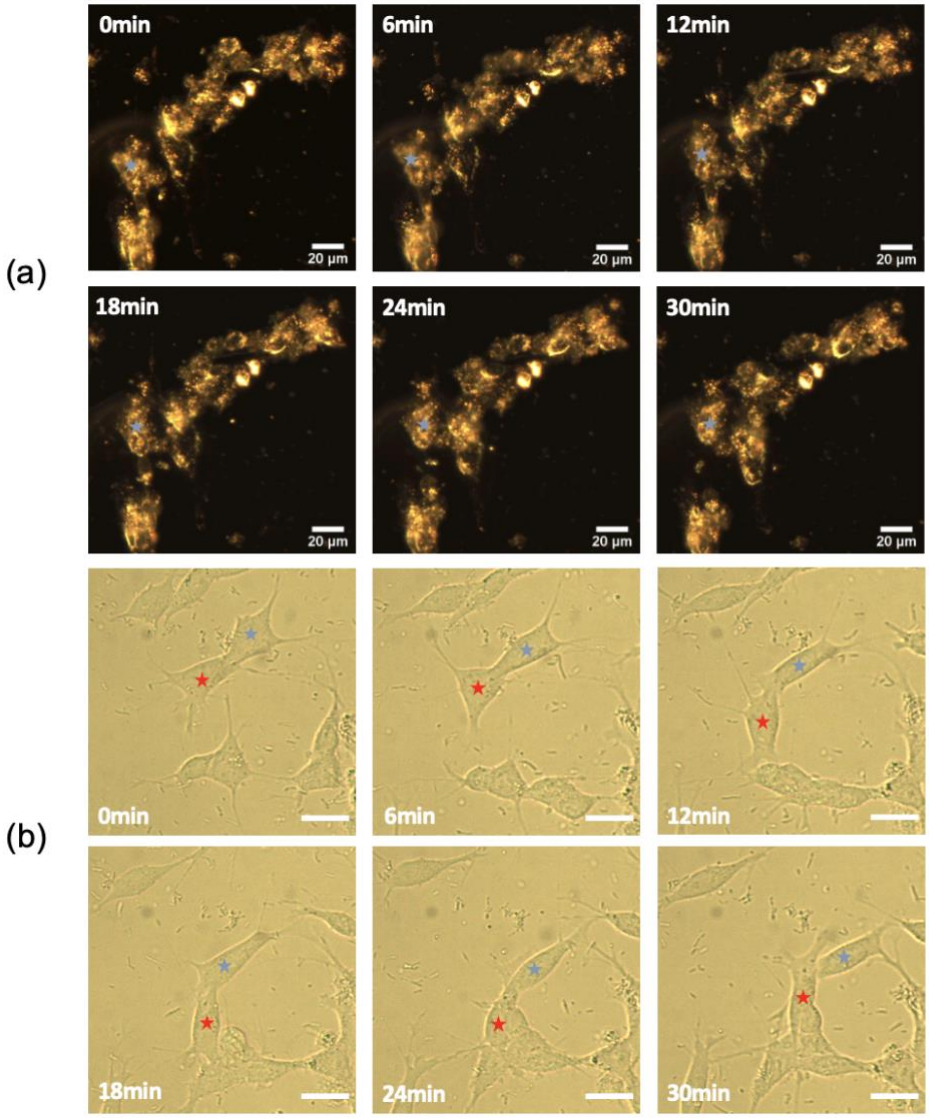

Appendix Figure B.1: SH-SY5Y cell migration observed in cell imaging chamber for 30 min. (a) GNR labeled cell (one cell indicated by blue star). (b) Negative control group (two cells indicated by red and blue stars). Scale bar: 20 μm.

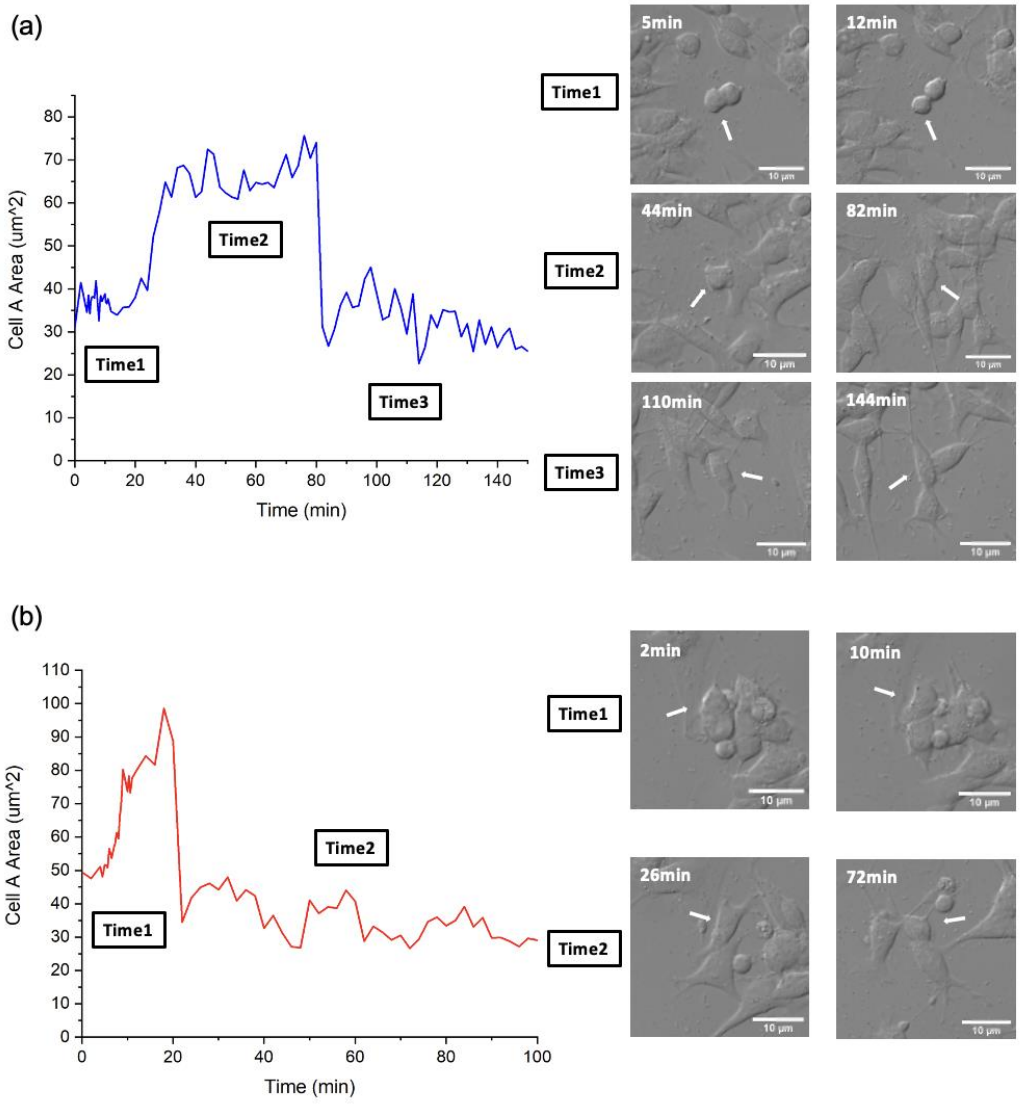

Appendix Figure B.2: SH-SY5Y cell division observed in cell imaging chamber for 144 min (a) and for 72 min (b). Cell area (μm^2) vs Time (min) of selected cells (indicated by white arrow) were measured and plotted. Scale bar: 10 μm.

BIBLIOGRAPHY

1. Chambers, I. *et al.* Nanog safeguards pluripotency and mediates germline development. *Nature* **450**, 1230–1234 (2007).
2. Paul, F. *et al.* Transcriptional Heterogeneity and Lineage Commitment in Myeloid Progenitors. *Cell* **163**, 1663–1677 (2015).
3. Bendall, S. C. *et al.* Single-cell trajectory detection uncovers progression and regulatory coordination in human b cell development. *Cell* **157**, 714–725 (2014).
4. Schulte, R. *et al.* Index sorting resolves heterogeneous murine hematopoietic stem cell populations. *Exp Hematol* **43**, 803–811 (2015).
5. Scialdone, A. *et al.* Resolving early mesoderm diversification through single-cell expression profiling. *Nature* **535**, 289–293 (2016).
6. Skylaki, S., Hilsenbeck, O. & Schroeder, T. Challenges in long-term imaging and quantification of single-cell dynamics. *Nat Biotechnol* **34**, 1137–1144 (2016).
7. Schroeder, T. Long-term single-cell imaging of mammalian stem cells. *Nat Methods* **8**, S30–S35 (2011).
8. Schroeder, T. Tracking Hematopoiesis at the Single Cell Level. *Ann N Y Acad Sci* **1044**, 201–209 (2005).
9. Hoppe, P. S. *et al.* Early myeloid lineage choice is not initiated by random PU.1 to GATA1 protein ratios. *Nature* **535**, 299–302 (2016).
10. Widengren, J. & Rigler, R. Mechanisms of photobleaching investigated by fluorescence correlation spectroscopy. *Bioimaging* **4**, 149–157 (1996).
11. Takizawa, T. & Robinson, J. M. Analysis of antiphotobleaching reagents for use with FluoroNanogold in correlative microscopy. *Journal of Histochemistry and Cytochemistry* **48**, 433–436 (2000).
12. Schroeder, T. Imaging stem-cell-driven regeneration in mammals. *Nature* **453**, 345–351 (2008).
13. Coutu, D. L. & Schroeder, T. Probing cellular processes by long-term live imaging - historic problems and current solutions. *J Cell Sci* **126**, 3805–3815 (2013).
14. Lin, W. K. *et al.* Optically and Structurally Stabilized Plasmo-Bio Interlinking Networks. *Adv Mater Interfaces* **8**, (2021).
15. Kokkaliaris, K. D. *et al.* Identification of factors promoting ex vivo maintenance of mouse hematopoietic stem cells by long-term single-cell quantification. *Blood, The Journal of the American Society of Hematology* **128**, 1181–1192 (2016).

16. Vedel, S., Tay, S., Johnston, D. M., Bruus, H. & Quake, S. R. Migration of Cells in a Social Context. *Biophys J* **104**, 147a (2013).

17. Keren, K. *et al.* Mechanism of shape determination in motile cells. *Nature* **453**, 475–480 (2008).

18. Kellogg, R. A., Gómez-Sjöberg, R., Leyrat, A. A. & Tay, S. High-throughput microfluidic single-cell analysis pipeline for studies of signaling dynamics. *Nat Protoc* **9**, 1713–1726 (2014).

19. Huang, B., Bates, M. & Zhuang, X. Super-Resolution Fluorescence Microscopy. *Annu Rev Biochem* **78**, 993–1016 (2009).

20. Leung, B. & Chou, K. Review of Super- Resolution Fluorescence Microscopy for Biology. *Appl Spectrosc* **65**, 967–980 (2011).

21. Zhanghao, K. *et al.* Super-resolution imaging of fluorescent dipoles via polarized structured illumination microscopy. *Nat Commun* **10**, (2019).

22. Culley, S. *et al.* Quantitative mapping and minimization of super-resolution optical imaging artifacts. *Nature Publishing Group* **15**, 263–266 (2018).

23. Klar, T. A. & Hell, S. W. Subdiffraction resolution in far-field fluorescence microscopy. *Opt Lett* **24**, (1999).

24. Hell, S. W. & Kroug, M. Ground-state-depletion fluorscence microscopy: a concept for breaking the diffraction resolution limit. *Appl. Phys. B* **60**, 495–497 (1995).

25. Michael Hofmann, Christian Eggeling, Stefan Jakobs & Stefan W. Hell. Breaking the diffraction barrier in fluorescence microscopy at low light intensities by using reversibly photoswitchable proteins. *Proceedings of the National Academy of Sciences* **102**, 17565–17569 (2005).

26. T. Dertinger, R. Colyer, G. Iyer, S. Weiss & J. Enderlein. Fast, background-free, 3D super-resolution optical fluctuation imaging (SOFI). *Proceedings of the National Academy of Sciences* **106**, 22287–22292 (2009).

27. Lemmer, P. *et al.* SPDM: Light microscopy with single-molecule resolution at the nanoscale. *Appl Phys B* **93**, 1–12 (2008).

28. Betzig, E. *et al.* Imaging Intracellular Fluorescent Proteins at Nanometer Resolution. *Science (1979)* **313**, 1642–1645 (2006).

29. Rust, M. J., Bates, M. & Zhuang, X. Sub-diffraction-limit imaging by stochastic optical reconstruction microscopy (STORM). *Nat Methods* **3**, 793–795 (2006).

30. Yu, Y.-Y., Chang, S.-S., Lee, C.-L. & Wang, C. R. C. Gold Nanorods: Electrochemical Synthesis and Optical Properties. *J Phys Chem B* **101**, 6661–6664 (1997).

31. Nikoobakht, B. & El-Sayed, M. A. Preparation and growth mechanism of gold nanorods (NRs) using seed-mediated growth method. *Chemistry of Materials* **15**, 1957–1962 (2003).

32. Murphy, C. J. *et al.* Anisotropic metal nanoparticles: Synthesis, assembly, and optical applications. *Journal of Physical Chemistry B* **109**, 13857–13870 (2005).

33. Oldenburg, S. J., Averitt, R. D., Westcott, S. L. & Halas, N. J. Nanoengineering of optical resonances. *Chem Phys Lett* **288**, 243–247 (1998).

34. Sun, Y., Mayers, B. T. & Xia, Y. Template-Engaged Replacement Reaction: A One-Step Approach to the Large-Scale Synthesis of Metal Nanostructures with Hollow Interiors. *Nano Lett* **2**, 481–485 (2002).

35. Mie, Gustav. A contribution to the optics of turbid media, especially colloidal metallic suspensions. *Ann. Phys* **25**, 377–445 (1908).

36. Petryayeva, E. & Krull, U. J. Localized surface plasmon resonance: Nanostructures, bioassays and biosensing-A review. *Anal Chim Acta* **706**, 8–24 (2011).

37. Mayer, K. M. & Hafner, J. H. Localized surface plasmon resonance sensors. *Chem Rev* **111**, 3828–3857 (2011).

38. Cao, J., Sun, T. & Grattan, K. T. V. Gold nanorod-based localized surface plasmon resonance biosensors: A review. *Sens Actuators B Chem* **195**, 332–351 (2014).

39. Gans, R. Über die form ultramikroskopischer goldteilchen. *Ann Phys* **342**, 881–900 (1912).

40. Hu, M. *et al.* Gold nanostructures: Engineering their plasmonic properties for biomedical applications. *Chem Soc Rev* **35**, 1084–1094 (2006).

41. Pérez-Juste, J., Pastoriza-Santos, I., Liz-Marzán, L. M. & Mulvaney, P. Gold nanorods: Synthesis, characterization and applications. *Coord Chem Rev* **249**, 1870–1901 (2005).

42. Link, S., Mohamed, M. B. & El-Sayed, M. A. Simulation of the optical absorption spectra of gold nanorods as a function of their aspect ratio and the effect of the medium dielectric constant. *Journal of Physical Chemistry B* **103**, 3073–3077 (1999).

43. Jain, P. K., Lee, K. S., El-Sayed, I. H. & El-Sayed, M. A. Calculated absorption and scattering properties of gold nanoparticles of different size, shape, and composition: Applications in biological imaging and biomedicine. *Journal of Physical Chemistry B* **110**, 7238–7248 (2006).

44. Huang, X. & El-sayed, M. A. Gold nanoparticles : Optical properties and implementations in cancer diagnosis and photothermal therapy. *J Adv Res* **1**, 13–28 (2010).

45. Chang, W.-S., Ha, J. W., Slaughter, L. S. & Link, S. Plasmonic nanorod absorbers as orientation sensors. *Proceedings of the National Academy of Sciences* **107**, 2781–2786 (2010).

46. Hayden, J. E. Adventures on the Dark Side: An Introduction to Darkfield Microscopy. *Biotechniques* **32**, 756–761 (2002).

47. Liu, M. *et al.* Dark-field microscopy in imaging of plasmon resonant nanoparticles. *Colloids Surf B Biointerfaces* **124**, 111–117 (2014).

48. Cui, G. *et al.* Phase intensity nanoscope (PINE) opens long-time investigation windows of living matter. *Nat Commun* **14**, (2023).

49. Beck, A. & Teboulle, M. A fast iterative shrinkage-thresholding algorithm for linear inverse problems. *SIAM J Imaging Sci* **2**, 183–202 (2009).

50. A. Leeuwenhoek. Cytosol. Cytoskeleton. in *Atlas of plant and animal histology* (2016).

51. Wioland, H., Jegou, A. & Romet-Lemonne, G. Torsional stress generated by ADF/cofilin on cross-linked actin filaments boosts their severing. *Proc Natl Acad Sci U S A* **116**, 2595–2602 (2019).

52. Hao, Y. K., Charras, G. T., Mitchison, T. J. & Brieher, W. M. Actin disassembly by cofilin, coronin, and Aip1 occurs in bursts and is inhibited by barbed-end cappers. *Journal of Cell Biology* **182**, 341–353 (2008).

53. Iwase, T., Sasaki, Y. & Hatori, K. Alignment of actin filament streams driven by myosin motors in crowded environments. *Biochim Biophys Acta Gen Subj* **1861**, 2717–2725 (2017).

54. Perico, C. & Sparkes, I. Plant organelle dynamics: cytoskeletal control and membrane contact sites. *New Phytologist* **220**, 381–394 (2018).

55. Harvey Lodish, Arnold Berk, Chris A. Kaiser & Monty Krieger. *Molecular Cell Biology*. (Macmillan, 2008).

56. Holmes, K. C., Popp, D., Gebhard, W. & Kabsch, W. Atomic model of the actin filament. *Nature* **347**, 44–49 (1990).

57. Zimmerle, C. T. & Frieden, C. Effect of pH on the Mechanism of Actin Polymerization. *Biochemistry* **27**, 7766–7772 (1988).

58. Bruce Alberts *et al.* The Self-Assembly and Dynamic Structure of Cytoskeletal Filaments. in *Molecular Biology of the Cell* (Garland Science, 2002).

59. Wioland, H., Jegou, A. & Romet-Lemonne, G. Torsional stress generated by ADF/cofilin on cross-linked actin filaments boosts their severing. *Proc Natl Acad Sci U S A* **116**, 2595–2602 (2019).

60. McGough, A., Pope, B., Chiu, W., Weeds, A. & McLean, M. Cofilin Changes the Twist of F-Actin: Implications for Actin Filament Dynamics and Cellular Function. *J Cell Biol* **138**, 771–781 (1997).

61. Luxenburg, C., Amalia Pasolli, H., Williams, S. E. & Fuchs, E. Developmental roles for Srf, cortical cytoskeleton and cell shape in epidermal spindle orientation. *Nat Cell Biol* **13**, 203–214 (2011).

62. Gibieža, P. & Petrikaitė, V. The regulation of actin dynamics during cell division and malignancy. *Am J Cancer Res* **11**, 4050–4069 (2021).

63. Pavel D. Hrdina. Basic Neurochemistry: Molecular, Cellular and Medical Aspects. *Journal of Psychiatry and Neuroscience* **21**, 352–353 (1996).

64. Irwin B Levitan & Leonard K. Kaczmarek. *The Neuron: Cell and Molecular Biology*. (Oxford University Press, 2015).

65. Gordon Macpherson. *Black's Medical Dictionary*. (A&C Black, 2002).

66. Biedler1, J. L., Roffler-Tarlov, S., Schachner, M. & Freedman, L. S. Multiple Neurotransmitter Synthesis by Human Neuroblastoma Cell Lines and Clones. *Cancer Res* **38**, 3751–3757 (1978).

67. Phhlman, S., Ruusala, A.-I., Abrahamsson, L., Mattsson, M. E. K. & Esscher, T. Retinoic acid-induced differentiation of cultured human neuroblastoma cells: a comparison with phorbolester-induced differentiation. *Cell Differ* **14**, 135–144 (1984).

68. Adem, A., Mattsson, M. E. K., Nordberg, A. & Hlman, S. P. Muscarinic receptors in human SH-SY5Y neuroblastoma cell line: regulation by phorbol ester and retinoic acid-induced differentiation. *Developmental Brain Research* **33**, 235–242 (1987).

69. Melino, G., Thiele, C. J., Knight, R. A. & Piacentini, M. Retinoids and the control of growth/death decisions in human neuroblastoma cell lines. *J Neurooncol* **31**, 65–83 (1997).

70. Jane Kovalevich & Dianne Langford. *Considerations for the Use of SH-SY5Y Neuroblastoma Cells in Neurobiology*. (Springer Protocols, 2013).

71. Ralph A. Bradshaw & Edward A. Dennis. *Handbook of Cell Signaling*. vol. 1 (Academic, 2009).

72. Govek, E. E., Newey, S. E. & Van Aelst, L. The role of the Rho GTPases in neuronal development. *Genes Dev* **19**, 1–49 (2005).

73. Encinas, M. *et al.* Sequential treatment of SH-SY5Y cells with retinoic acid and brain-derived neurotrophic factor gives rise to fully differentiated, neurotrophic factor-dependent, human neuron-like cells. *J Neurochem* **75**, 991–1003 (2000).

74. Laifenfeld, D., Klein, E. & Ben-Shachar, D. Norepinephrine alters the expression of genes involved in neuronal sprouting and differentiation: Relevance for major depression and antidepressant mechanisms. *J Neurochem* **83**, 1054–1064 (2002).

75. Presgraves, S. P., Ahmed, T., Borwege, S. & Joyce, J. N. Terminally Differentiated SH-SY5Y Cells Provide a Model System for Studying Neuroprotective Effects of Dopamine Agonists. *Neurotox Res* **5**, 579–598 (2004).

76. Nicolini, G. *et al.* Retinoic acid differentiated SH-SY5Y human neuroblastoma cells: an in vitro model to assess drug neurotoxicity. *Anticancer Res* **18**, 2477—2481 (1998).

77. Maruyama, W., Strolin Benedetti, M., Takahashi, T. & Naoi, M. A neurotoxin N-methyl(R)salsolinol induces apoptotic cell death in differentiated human dopaminergic neuroblastoma SH-SY5Y cells. *Neurosci Lett* **232**, 147–150 (1997).

78. R. Constantinescu, A. T. Constantinescu, H. Reichmann & B. Janetzky. *Neuronal Differentiation and Long-Term Culture of the Human Neuroblastoma Line SH-SY5Y*. (Springer Vienna, 2007).

79. Oosterheert, W., Klink, B. U., Belyy, A., Pospich, S. & Raunser, S. Structural basis of actin filament assembly and aging. *Nature* **611**, 374–379 (2022).

80. Ye, X. *et al.* Seeded growth of monodisperse gold nanorods using bromide-free surfactant mixtures. *Nano Lett* **13**, 2163–2171 (2013).

81. Wijaya, A. & Hamad-Schifferli, K. Ligand customization and DNA functionalization of gold nanorods via round-trip phase transfer ligand exchange. *Langmuir* **24**, 9966–9969 (2008).

82. Casas, J., Venkataramasubramani, M., Wang, Y. & Tang, L. Replacement of cetyltrimethylammoniumbromide bilayer on gold nanorod by alkanethiol crosslinker for enhanced plasmon resonance sensitivity. *Biosens Bioelectron* **49**, 525–530 (2013).

83. Busch, R. T. *et al.* Optimization and Structural Stability of Gold Nanoparticle-Antibody Bioconjugates. *ACS Omega* **4**, 15269–15279 (2019).

84. Golde, T. *et al.* Glassy dynamics in composite biopolymer networks. *Soft Matter* **14**, 7970–7978 (2018).

85. Sackmann, E., Bausch, E. & Vonna, L. Physics of Composite Cell Membrane and Actin Based Cytoskeleton. in *Physics of bio-molecules and cells* 237–284 (2002).

86. Liu, Y. *et al.* Rapid Depolarization-Free Nanoscopic Background Elimination of Cellular Metallic Nanoprobes. *Advanced Intelligent Systems* **4**, (2022).

87. Wang, Y., Liu, Y., Zhao, X. & Lee, S. E. High-speed nano-polarimetry for real-time plasmonic bio-imaging. in *Plasmonics in Biology and Medicine XV. Vol. 10509* 46–53 (2018).

88. Cooper, J. A., Walker, S. B. & Pollard, T. D. Pyrene actin: documentation of the validity of a sensitive assay for actin polymerization. *J Muscle Res Cell Motil* **4**, 253–262 (1983).

89. Quinlan, M. E., Heuser, J. E., Kerkhoff, E. & Dyche Mullins, & R. Drosophila Spire is an actin nucleation factor. *Nature* **433**, 382–388 (2005).

90. Scott D. Hansen, J. Bradley Zuchero, and R. D. M. Cytoplasmic Actin: Purification and Single Molecule Assembly Assays. *Adhesion Protein Protocols* 145–170 (2013).

91. Lieleg, O., Kayser, J., Brambilla, G., Cipelletti, L. & Bausch, A. R. Slow dynamics and internal stress relaxation in bundled cytoskeletal networks. *Nat Mater* **10**, 236–242 (2011).

92. Breitsprecher, D. *et al.* Cofilin cooperates with fascin to disassemble filopodial actin filaments. *J Cell Sci* **124**, 3305–3318 (2011).

93. Claessens, M. M. A. E., Bathe, M., Frey, E. & Bausch, A. R. Actin-binding proteins sensitively mediate F-actin bundle stiffness. *Nat Mater* **5**, 748–753 (2006).

94. Robaszkiewicz, K., Śliwinska, M. & Moraczewska, J. Regulation of actin filament length by muscle isoforms of tropomyosin and cofilin. *Int J Mol Sci* **21**, 1–19 (2020).

95. Schaller, V., Weber, C., Semmrich, C., Frey, E. & Bausch, A. R. Polar patterns of driven filaments. *Nature* **467**, 73–77 (2010).

96. Sarkar, A. & Daniels-Race, T. Electrophoretic deposition of carbon nanotubes on 3-amino-propyl-triethoxysilane (Aptes) surface functionalized silicon substrates. *Nanomaterials* **3**, 272–288 (2013).

97. Han Yuan Kueh, William M. Brieher, and T. J. M. Dynamic stabilization of actin filaments. *Proc. Natl. Acad. Sci. USA* **105**, 16531 (2008).

98. Wisanpitayakorn, P., Mickolajczyk, K. J., Hancock, W. O., Vidali, L. & Tüzel, E. Measurement of the Persistence Length of Cytoskeletal Filaments using Curvature Distributions. *Biophys J* **112**, 566a (2017).

99. Zhang, Z. *et al.* Dynamic observations of CRISPR-Cas target recognition and cleavage heterogeneities. *Nanophotonics* **11**, 4419–4425 (2022).

100. Feynman, R. P. *The Brownian Movement*. (Basic Books, 2004).

101. Los, D. A. & Murata, N. Membrane fluidity and its roles in the perception of environmental signals. *Biochim Biophys Acta* **1666**, 142–157 (2004).

102. Quinn, P. J. Effects of temperature on cell membranes. *Symp Soc Exp Biol* **42**, 237—258 (1988).

103. R. Ian Freshney. *Culture of Animal Cells: A Manual of Basic Technique and Specialized Applications*. (John Wiley & Sons, 2015).

104. Boyun Guo & Ali Ghalambor. *Natural Gas Engineering Handbook*. (Elsevier, 2014).

105. Korade, Z. & Kenworthy, A. K. Lipid rafts, cholesterol, and the brain. *Neuropharmacology* **55**, 1265–1273 (2008).

106. Frederick, R. L. & Shaw, J. M. Moving mitochondria: Establishing distribution of an essential organelle. *Traffic* **8**, 1668–1675 (2007).

107. Dong, C., Loy, C. C., He, K. & Tang, X. Image Super-Resolution Using Deep Convolutional Networks. *IEEE Trans Pattern Anal Mach Intell* **38**, 295–307 (2016).

108. Ledig, C. *et al.* Photo-Realistic Single Image Super-Resolution Using a Generative Adversarial Network. in *Proceedings of the IEEE conference on computer vision and pattern recognition* 4681–4690 (2017).